© 2020. Published by The Company of Biologists Ltd | Journal of Cell Science (2020) 133, jcs239202. doi:10.1242/jcs.239202

RESEARCH ARTICLE

The F1 loop of the talin head domain acts as a gatekeeper in integrin activation and clustering

Sampo Kukkurainen[1,2], Latifeh Azizi[1,2,*], Pingfeng Zhang[3,*], Marie-Claude Jacquier[4,*], Mo Baikoghli[5], Magdaléna von Essen[1,2], Anne Tuukkanen[6,7], Mikko Laitaoja[8], Xiaonan Liu[9], Rolle Rahikainen[1,2], Adam Orłowski[9], Janne Jänis[8], Juha A. E. Määttä[1,2], Markku Varjosalo[9], Ilpo Vattulainen[10,11], Tomasz Róg[10,11], Dmitri Svergun[6], R. Holland Cheng[5], Jinhua Wu[3], Vesa P. Hytönen[1,2,‡,§] and Bernhard Wehrle-Haller[4,‡,§]

ABSTRACT

Integrin activation and clustering by talin are early steps of cell adhesion. Membrane-bound talin head domain and kindlin bind to the β integrin cytoplasmic tail, cooperating to activate the heterodimeric integrin, and the talin head domain induces integrin clustering in the presence of Mn^{2+}. Here we show that kindlin-1 can replace Mn^{2+} to mediate β3 integrin clustering induced by the talin head, but not that induced by the F2–F3 fragment of talin. Integrin clustering mediated by kindlin-1 and the talin head was lost upon deletion of the flexible loop within the talin head F1 subdomain. Further mutagenesis identified hydrophobic and acidic motifs in the F1 loop responsible for β3 integrin clustering. Modeling, computational and cysteine crosslinking studies showed direct and catalytic interactions of the acidic F1 loop motif with the juxtamembrane domains of α- and β3-integrins, in order to activate the β3 integrin heterodimer, further detailing the mechanism by which the talin–kindlin complex activates and clusters integrins. Moreover, the F1 loop interaction with the β3 integrin tail required the newly identified compact FERM fold of the talin head, which positions the F1 loop next to the inner membrane clasp of the talin-bound integrin heterodimer.

This article has an associated First Person interview with the first author of the paper.

KEY WORDS: Activation, Cell adhesion, Clustering, Integrin, Molecular dynamics, Talin

[1]Faculty of Medicine and Health Technology, Tampere University, Arvo Ylpön katu 34, FI-33520 Tampere, Finland. [2]Fimlab Laboratories, Biokatu 4, FI-33520 Tampere, Finland. [3]Molecular Therapeutics Program, Fox Chase Cancer Center, Philadelphia, PA 19111, USA. [4]Department of Cell Physiology and Metabolism, University of Geneva, Centre Médical Universitaire, Rue Michel-Servet 1, 1211 Geneva 4, Switzerland. [5]Department of Molecular and Cellular Biology, University of California, 1 Shields Ave, Davis, CA 95616, USA. [6]EMBL Hamburg c/o DESY, European Molecular Biology Laboratory, Notkestrasse 85, 22607 Hamburg, Germany. [7]European Bioinformatics Institute (EMBL-EBI), European Molecular Biology Laboratory, Wellcome Genome Campus, Hinxton, Cambridgeshire CB10 1SD, UK. [8]Department of Chemistry, University of Eastern Finland, P.O. Box 111, FI-80101 Joensuu, Finland. [9]Proteomics Unit, Institute of Biotechnology, University of Helsinki, FI-00014 Helsinki, Finland. [10]Computational Physics Laboratory, Tampere University, FI-33520 Tampere, Finland. [11]Department of Physics, University of Helsinki, P.O. Box 64, FI-00014 Helsinki, Finland.
*,‡These authors contributed equally to this work

[§]Authors for correspondence (Bernhard.Wehrle-Haller@unige.ch; Vesa.Hytonen@tuni.fi)

S.K., 0000-0002-0635-784X; P.Z., 0000-0001-5985-4914; M.v.E., 0000-0002-2412-6316; M.V., 0000-0002-1340-9732; I.V., 0000-0001-7408-3214; J.W., 0000-0001-5913-0633; V.P.H., 0000-0002-9357-1480; B.W., 0000-0002-1159-1147

Handling Editor: Michael Way
Received 12 September 2019; Accepted 31 July 2020

INTRODUCTION

Cells spread, adhere and move with the help of integrins. Integrins are allosterically regulated heterodimeric transmembrane receptors forming 24 distinct combinations of α- and β-integrins in mammals (Hynes, 2002; Bachmann et al., 2019). Cytoplasmic adaptor proteins, along with extracellular divalent cations and tensional forces, affect integrin conformation and interactions with extracellular ligands (Sun et al., 2016; Bachmann et al., 2019). One of the key intracellular adaptors is talin, a large, modular protein that binds and activates integrins with its N-terminal head domain, while connecting them to actin fibers via its C-terminal rod domain, which harbors binding sites for further adaptor and signaling molecules required to form cell–matrix adhesion complexes (Sun et al., 2016; Haining et al., 2016). Humans have two talins, talin-1 and talin-2, which have 76% amino acid sequence identity. Of these two talin forms, talin-1 is ubiquitously expressed and is critical for cell adhesion and morphogenesis (Monkley et al., 2000, 2011; Calderwood et al., 2013; Ellis et al., 2013), whereas talin-2 is highly expressed in brain and striated muscle (Senetar and McCann, 2005; Senetar et al., 2007; Debrand et al., 2012). Hereafter, the term talin refers to talin-1.

The talin N-terminal head domain (defined by calpain II cleavage at residues 433–435) contains two ubiquitin-like subdomains (F0 and F1), an acyl-coenzyme A-binding protein-like subdomain (F2) and a phosphotyrosine binding-like integrin-binding subdomain (F3) (Roberts and Critchley, 2009), followed by a calpain II processable linker (residues 406–481) (Rees et al., 1990). The C-terminal rod domain (residues 482–2541) is composed of 13 α-helical bundles that bind actin filaments and adaptor proteins, and a C-terminal helix involved in talin dimerization (Roberts and Critchley, 2009; Gingras et al., 2008; Calderwood et al., 2013). Association with phosphatidylinositol (4,5)-bisphosphate (PIP2)-containing membranes regulates talin activity and integrin binding by competing with auto-inhibitory rod bundle–head domain interactions (Goksoy et al., 2008; Saltel et al., 2009; Goult et al., 2013; Zhang et al., 2016). The talin head domain is a FERM domain by homology (residues 84–405), and talin-1 has been crystallized in a linear arrangement of the subdomains (Elliott et al., 2010; Chinthalapudi et al., 2018). A talin-2 structure adopting a novel cloverleaf-like conformation was presented recently (Rangarajan et al., 2020).

In addition to talin, knockout studies of kindlin-1, -2 and -3 (also known as FERMT1, 2 and 3, respectively), as well as studies of patients with kindlin-3 deficiencies have shown that kindlins are also required for integrin activation and clustering (Montanez et al., 2008; Moser et al., 2008; Qu et al., 2011; Theodosiou et al., 2016). However, in most experimental settings, endogenous kindlin is present in cells, and hence integrins can be activated by talin head overexpression (Tadokoro et al., 2003). Integrins can also be allosterically activated by ligand binding and manganese (Mn^{2+})

Journal of Cell Science (2020) 133, jcs239202. doi:10.1242/jcs.239202

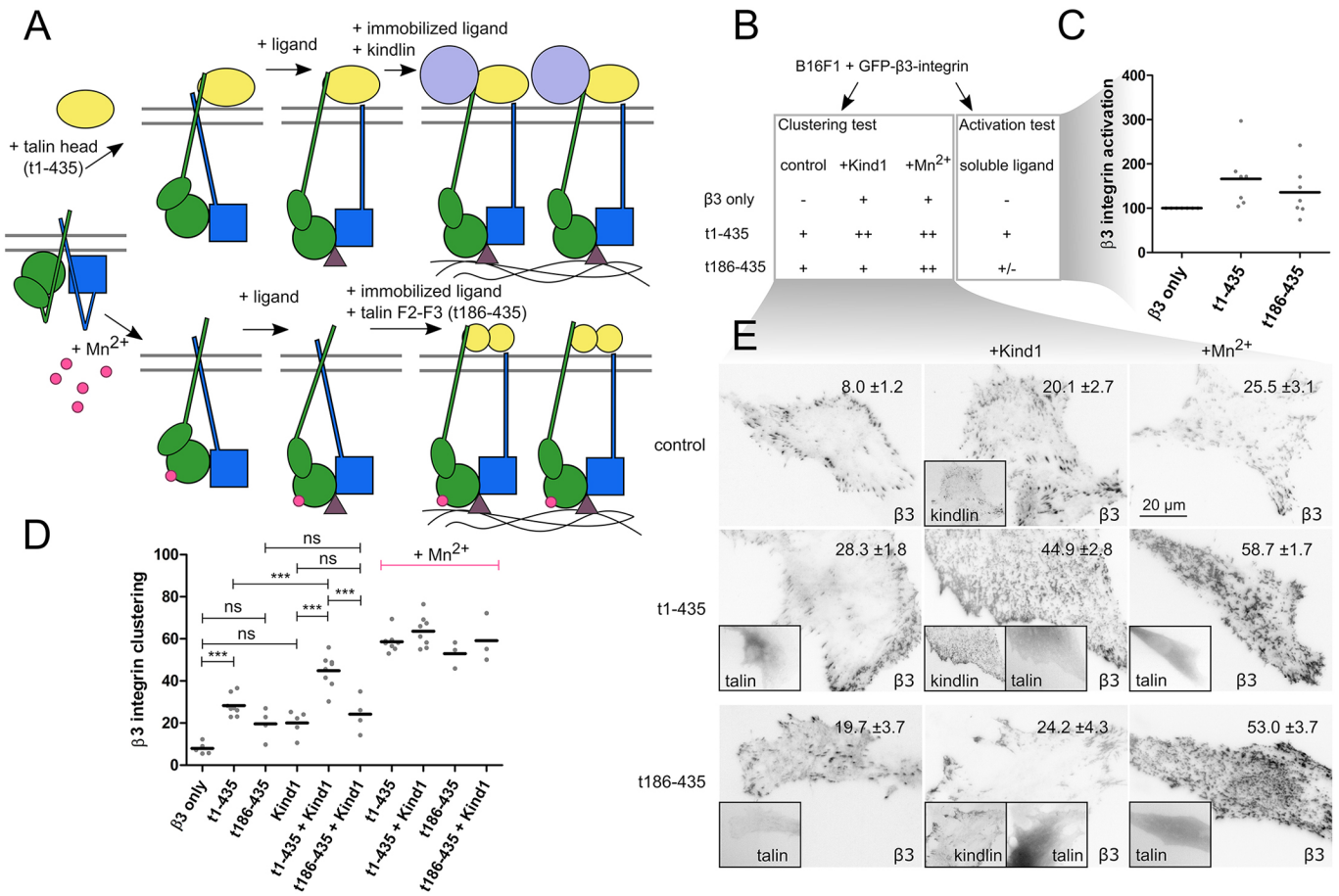

Fig. 1. The complete talin head cooperates with kindlin to activate αvβ3 integrin. Integrin activation and clustering by the complete (subdomains F0–F3, residues 1–435) or partial talin head (subdomains F2–F3, residues 186–435) in B16F1 cells co-transfected with β3–GFP integrin are visualized schematically in (A) and presented as a table in (B). In A: green, α-integrin; blue, β-integrin; yellow, talin head domain; light blue, kindlin; purple triangle, integrin ligand; pink sphere, manganese ion. In B, the scoring for clustering is as follows: - (clustering index 0-10), + (10-30), ++ (>30). Scoring for activation: - (basal level), +/- (activation increase <50%), + (activation increase >50%). Kind1, kindlin-1. (C) Integrin activation assay. Soluble RGD-ligand (SKI-7) binding to B16F1 cells co-transfected with β3–GFP integrin and complete and partial CFP-labeled talin head (t1–435, *n*=7 experiments; t186–435, *n*=7). The control cells (β3 only, *n*=7 experiments) expressed β3–GFP integrin. Dots indicate activation indices (percentage relative to the control), and lines indicate mean values. Variation between the groups was determined using a one-way ANOVA [$F(2,18)=3.04$]. Despite the differences in the mean activation levels, the variance analysis revealed no significant difference. (D) β3–GFP integrin clustering assay. Clustering indices and mean values are shown. The differences in clustering efficiency were analyzed by one-way ANOVA [$F(9,46)=48.99$, $P<0.0001$] and Tukey's multiple comparison test. ***$P<0.001$; ns, not significant. Among the Mn^{2+}-treated groups (magenta), no significant differences in β3–GFP integrin clustering efficiency were found. The numbers of experiments (15–25 cells evaluated per experiment) in the non-Mn^{2+}-treated group were: β3 only, *n*=5; t1–435, *n*=8; t186–435, *n*=4; Kind1, *n*=5; t1–435+Kind1, *n*=8; and t186–435+Kind1, *n*=4. For the manganese-treated group the numbers of experiments were: t1–435, *n*=8; t1–435+Kind1, *n*=8; t186–435, *n*=3; and t186–435+Kind1, *n*=3. (E) TIRF images (kindlin-1, β3 integrin) and epifluorescence of transfected talin head constructs showing the representative integrin phenotypes, along with clustering indices (mean±s.d.). For Mn^{2+} alone, images are representative of *n*=5 experiments. Scale bar: 20 µm.

(Mould et al., 1995; Eng et al., 2011) (Fig. 1A). Upon binding to bent integrins on the cell surface, Mn^{2+} switches integrins to an extended conformation, allowing interaction with immobilized extracellular ligands, leading to integrin clustering in a talin-head-dependent manner (Cluzel et al., 2005; Saltel et al., 2009; Changede et al., 2015; Bachmann et al., 2019). For this talin-head-dependent integrin clustering to occur, an acidic (D723/E726), membrane-proximal motif in β3 integrins interacts with basic residues (K316/K324) in the talin F3 subdomain, while other basic residues of the F2 and F3 subdomains interact with acidic membrane lipids, such as PIP2 (Anthis et al., 2009; Saltel et al., 2009). The talin head subdomains F2 and F3 (referred to collectively as F2–F3) are hence sufficient for activation of αIIbβ3 integrin, as recorded using the PAC-1 antibody in detached cells (Tadokoro et al., 2003), but fail to activate α5β1 integrin, when probed with a fibronectin fragment (Bouaouina et al., 2008). This suggests that, at least in the latter case, the entire talin head domain is needed for the binding of soluble ligand. Importantly, when kindlin-1 and kindlin-2 are completely removed from cells, talin no longer activates integrins and cells do not spread (Theodosiou et al., 2016). In addition, Rap1 (RAP1A and RAP1B in mammals) binding to the F0 and/or F1 subdomains of the talin head has been proposed to recruit talin to the plasma membrane, contributing to integrin activation and Rap1-mediated cell–matrix adhesion (Camp et al., 2018; Katzemich et al., 2019; Gingras et al., 2019). Thus, talin, Rap1 and kindlin play important roles in the integrin activation step, while kindlin also induces clustering of activated integrins (Feigelson et al., 2011; Schmidt et al., 2011; Feng et al., 2012; Ye et al., 2013).

The F1 subdomains of both talins and kindlins contain a long loop (38 residues in talin) that binds to negatively charged membrane lipids (Goult et al., 2010; Bouaouina et al., 2012). The talin F1 loop is important for αIIbβ3- and α5β1-integrin activation,

Journal of Cell Science (2020) 133, jcs239202. doi:10.1242/jcs.239202

but not for β1 integrin binding to talin (Goult et al., 2010; Bouaouina et al., 2008). Charge inversion of basic residues in the talin F1 loop inhibits cell spreading (Elliott et al., 2010), membrane association of the F1 subdomain and integrin activation (Goult et al., 2010). Nevertheless, the F2–F3 subdomains alone bind efficiently to membranes, and the F0–F1 subdomains do not further enhance this interaction (Moore et al., 2012). In addition, the F1 loop is reportedly flexible and does not form stable contacts within the talin head, and its removal has not been found to affect the structure of the folded subdomains (Elliott et al., 2010). Thus, it is not fully clear how the F1 loop contributes to talin-head-induced integrin activation, since it also acts downstream of the Rap1-mediated mechanism of integrin activation and membrane recruitment (Gingras et al., 2019). Nevertheless, it appears to be a site of important posttranslational modifications, because phosphorylation of the F1 loop at T144 and T150 has been associated with reduced membrane binding (Goult et al., 2010), and also affects talin recruitment to muscle attachment sites in *Drosophila* (Katzemich et al., 2019).

Talin is, so far, the only FERM family protein that has not been shown to fold into a conserved cloverleaf-like shape, and current models propose that the membrane recruitment of the talin head domain in an F1 loop- and Rap1-dependent manner is the key to integrin activation. Here, we validated the FERM fold of the full-length talin head by small-angle X-ray scattering and used molecular dynamics (MD) analysis to evaluate the functional role of the F1 loop in integrin activation. We show that the F1 loop interacts with the β integrin cytoplasmic tail and interferes with the inner membrane clasp via conserved acidic residues, leading to integrin activation and clustering in a talin- and kindlin-mediated manner. Taken together, our data support a new mechanism for kindlin- and talin-induced integrin activation, in which the FERM-folded talin head tightly interacts with the β integrin tail and projects the F1 loop to act as a gatekeeper to control the talin–integrin association and regulate the activation and clustering of integrins.

RESULTS

Talin F1 loop is required for integrin activation and clustering

The talin head can induce integrin activation (as measured by soluble ligand binding) and integrin clustering (Tadokoro et al., 2003; Goult et al., 2010; Cluzel et al., 2005) (Fig. 1A). However, we found that the integrin-binding F2–F3 fragment of the talin head (t186–435), when probed with a soluble, RGD-containing snake venom (SKI-7; Ballestrem et al., 2001), did not efficiently activate β3 integrin (Fig. 1B,C). Similarly, the talin F2–F3 fragment is reportedly not sufficient to induce α5β1 integrin activation, when measured by soluble fibronectin binding (Bouaouina et al., 2008), whereas it activates αIIbβ3 integrin when probed with the multivalent PAC-1 IgM antibody (Calderwood et al., 2002; Tadokoro et al., 2003; Bouaouina et al., 2008). On the other hand, the talin head F2–F3 fragment induces αvβ3 integrin clustering on vitronectin-coated surfaces in the presence of Mn^{2+} (Saltel et al., 2009). Because integrin activation and clustering are tightly interlinked (Bunch, 2009), the conformational activation of the extracellular domain of integrins by Mn^{2+} may therefore mask the physiological role of the intracellular adaptors in the regulation of the integrin function at the cell surface.

In order to develop a more physiological Mn^{2+}-independent test that also takes into account the role of kindlin in integrin activation (Ma et al., 2008; Moser et al., 2009; Harburger et al., 2009), and therefore its potential influence on integrin clustering, we analyzed the clustering of β3 integrin with a C-terminal GFP tag (β3–GFP integrin) in the presence of fluorescently labeled talin head and kindlin-1 in B16F1 melanoma cells spread on serum-coated glass coverslips (Fig. 1B,C,D) (Saltel et al., 2009). The degree of clustering of integrin receptors was calculated from TIRF images, by determining the percentage of the cell area covered with integrin clusters (Fig. 1E). The complete talin head domain (t1–435) enhanced β3–GFP integrin clustering ($P<0.001$), but the co-expression of kindlin-1 with the talin head and β3–GFP integrin was needed for increasing the integrin clustering further ($P<0.001$) to a level similar to that observed with the talin head and Mn^{2+}. Interestingly, kindlin-1 did not enhance talin F2–F3-mediated clustering, whereas this did occur when Mn^{2+} was used for integrin activation (Saltel et al., 2009) (Fig. 1D,E). Importantly, co-expression of talin head and kindlin-1 was critical for full clustering. Although the exact role of kindlin in the integrin activation process is still unknown (Rognoni et al., 2016), kindlin-mediated integrin clustering requires the presence of the talin F0–F1 subdomains. In addition, the large loop insert in the F1 subdomain is a feature of talins and kindlins, and has been shown to be important for integrin activation by both adaptors (Goult et al., 2010; Bouaouina et al., 2012). Because antibody interference of the talin–integrin association using an F1 loop-directed monoclonal antibody, Ta205 (Xing et al., 2006), suggested proximity of the F1 loop to the integrin-binding F3 subdomain in the talin head, we decided to further investigate the role of the talin F1 loop in kindlin-1-assisted integrin clustering by assaying a series of loop deletions. In addition, we created a model of a FERM-folded talin head domain, containing the F1 loop, to study the biological role of the F1 loop *in silico* (Fig. 2).

We completely removed the talin F1 loop using two different strategies: by deleting residues 139–168 (del30), as was done for the previously published elongated structures of the talin head (Goult et al., 2010; Elliott et al., 2010), and by replacing residues 134–170 with a Gly-Ala-Gly stretch (del37/GAG) to yield a loop similar in sequence and equal in length to *Dictyostelium* TalB (Fig. 2G,H; Fig. S1). Both loop deletions led to defects in β3 integrin activation and clustering (Fig. 2F,H,I), but enhanced β3 integrin binding *in vitro* (Tables S1, S2). We then further narrowed down the deletion to the central part of the loop (del17), and replaced the residues 151–154 (LLRD) with four alanines (151–154AAAA), preserving the length, the previously identified cluster of basic residues (Goult et al., 2010) and the net charge of the loop. Neither of the mutants showed significant integrin activation (Fig. 2F), and the 151–154AAAA mutation alone was sufficient to decrease clustering as compared to the wild-type head domain (t1–435), suggesting that the central stretch of residues 151–154 (LLRD) is important for the functions of the F1 loop. Despite the presence of a full-size F1 loop, the 151–154AAAA mutant displayed decreased *in vitro* binding to β3 integrin compared to that of the F1 loop deletion mutants, and this was even slightly lower than measured for the wild-type F1 loop (Table S2). These data suggest that the F1 loop interferes with β3 integrin binding to the talin head, to some extent, but at the same time appears to stimulate integrin activation and clustering.

Modeling of the F1 loop into the compact talin FERM fold

Because all talin head structures published so far lack the F1 loop, we decided to create a F1 loop-containing talin head model based on the compact FERM fold and then explored its structural stability and potential lipid interactions using MD simulations. Compared to the existing extended crystal structure of the talin head [t1–400(del139–168/del30); PBD ID 3IVF] (Elliott et al., 2010), our talin model is rotated at its F1–F2 linker to yield a compact FERM domain (Fig. 2E), similar to the recently published crystallographic structure of kindlin-2 (PDB ID 5XPY) (Li et al., 2017). The F1 domain loop

Journal of Cell Science (2020) 133, jcs239202. doi:10.1242/jcs.239202

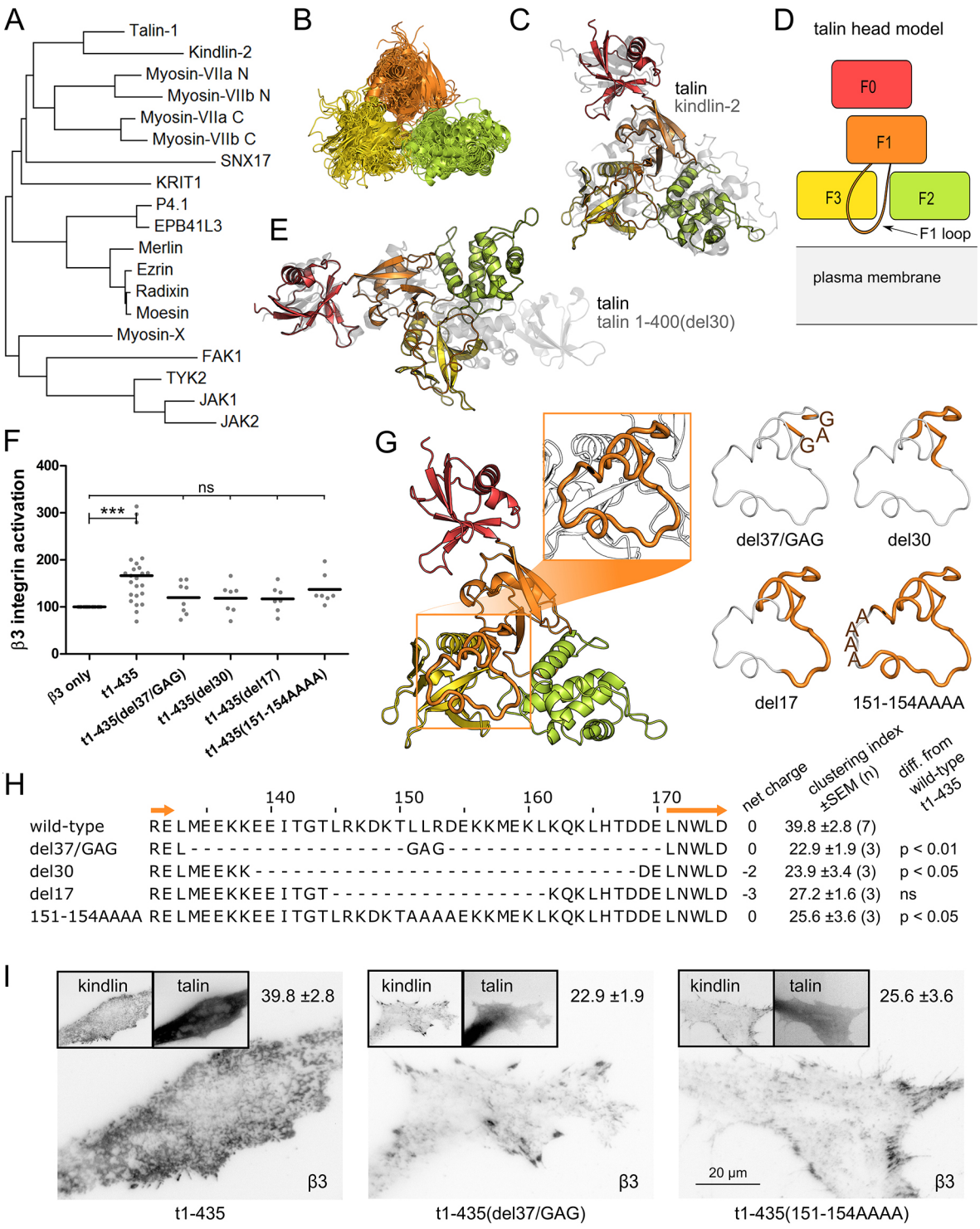

Fig. 2. See next page for legend.

conformation, adopted from a talin F1 subdomain NMR structure (PDB ID 2KC2) (Goult et al., 2010), is clearly different from the conformation of the F1 loop of kindlin-2. Similiar to the F1 loop in our talin model, the kindlin F1 loop is in contact with the F3 and F2 subdomains; however, the kindlin F1 loop is very long (~125 residues) compared to the talin loop (~40 residues).

Transmembrane and cytoplasmic domains of αIIbβ3 integrin and a lipid membrane were included in the MD simulation (Table S3). The talin head model remained in a stable FERM domain fold in all simulations except one, in which the F1–F2 interface slightly opened after 0.42 µs of simulation (PIP-A simulation; see Table S3). Generally, the F1, F2 and F3 subdomains remained in the FERM-like triangular assembly, with the F1 and F3 subdomains in contact and the F1 loop in close proximity to the integrin-binding site in the F3 subdomain throughout the 0.5–1 µs simulations. In this compact conformation, the talin head sat on the lipid membrane surface with lipid interaction sites in the F2 and F3 subdomains and in the F1 loop (Fig. S1). Whereas the F1 loop of an isolated F1 domain is

Journal of Cell Science (2020) 133, jcs239202. doi:10.1242/jcs.239202

Fig. 2. The talin head contains a FERM domain composed of F1, F2 and F3 subdomains, and a loop within the F1 subdomain is important for β3–GFP integrin activation and clustering. (A) Talin FERM domain similarity to known FERM domains from the proteins detailed Table S6 analyzed using the ProbCons algorithm (Do et al., 2005) via JalView (Waterhouse et al., 2009), and visualized as maximum likelihood tree calculated using MEGA7 (Kumar et al., 2016). P4.1, protein 4.1 (also known as ERB41). (B) The structures of the same FERM domains aligned in PyMOL (Schrodinger). (C) We constructed a FERM-folded talin head model, shown here superimposed with the crystal structure of kindlin-2 (Li et al., 2017) (gray) and revealed to be essentially identical to the FERM-folded structure (P.Z., L.A., S.K. et al., unpublished). (D) In addition to the F1, F2 and F3 subdomains of a FERM domain, talin contains an extra ubiquitin-like subdomain F0 and a loop of more than 30 residues inserted in the F1 subdomain. Subdomains F2, F3 and the F1 loop possess acidic lipid binding activities (Anthis et al., 2009; Saltel et al., 2009; Goult et al., 2010). (E) Comparison of the FERM-folded talin head model and the extended crystal structure of talin 1–400(del139–168) (gray; PDB ID 3IVF; Elliott et al., 2010). (F) Integrin activation assay. Soluble ligand (SKI-7) binding to B16F1 cells transfected with β3–GFP integrin and different CFP-labeled talin head versions. Dots indicate activation indices (percentage relative to the control), and lines indicate mean values. β3 only, n=26; t1–435, n=24; t1–435(del37/GAG), n=8; t1–435(del30), n=7; t1–435(del17), n=7; and t1–435(151–154AAAA), n=7. Variation between the groups was determined by one-way ANOVA [$F(5,73)=7.527$, $P<0.0001$] and Tukey's multiple comparison test, showing no significant difference (ns) between groups except for β3 only versus t1–435 (***$P\leq0.001$). (G) Localization of the F1 loop within the FERM domain model. The deleted loop regions (thin, gray backbone) are shown within the F1 loop (orange, thick backbone) on the right. The amino acid sequences of the F1 loop truncations are shown in H, presenting the F1 subdomain residues 131–175 of wild-type talin-1. β3–GFP integrin clustering indices of t1–435 talin head and its loop-modified forms are given next to the sequence alignment. Variation between groups was assessed with a one-way ANOVA [$F(5,16)=8.967$, $P=0.0003$] and Tukey's multiple comparison test (with 15–25 cells analyzed per experiment) to calculate the P-values indicated in the figure. The t1–435 only condition was used as control (mean±s.e.m.: 15.6±2.9, n=3). (I) Representative TIRF (kindlin-1, β3 integrin) and epifluorescence (talin) images, and mean±s.e.m. β3–GFP integrin clustering indices, of the wild-type talin head t1–435 and two loop-modified talin head forms are shown. Scale bar: 20 µm.

highly flexible (Goult et al., 2010), the compact, FERM-folded talin head stabilized the F1 loop conformation, with conserved regions of the loop contributing to interactions with integrin, talin head and lipids, as summarized in Fig. S1.

Talin F1 loop interacts directly with the inner membrane clasp of integrins

A salt bridge connects the αIIb and β3 integrin chains as part of the inner membrane clasp that controls integrin activation (Hughes et al., 1996; Anthis and Campbell, 2011). In the MD simulations, the talin F1 loop residue D154 competed with D723 of β3 integrin for binding to R995 of αIIb integrin (Fig. 3A–C), and a D154–R995 salt bridge formed after 3–180 ns (mean±s.d. distance between charged groups 3.5±0.3 Å). As a consequence, the contact between D723 and R995 was lost in all talin–integrin–lipid simulations (charged group distance 6.3±2.1 Å), whereas in control simulations without talin, the D723–R995 contacts were more stable (charged group distance 4.8±0.8 Å).

Based on the MD simulations, we hypothesized that a D154A substitution could block integrin clustering in cells. However, D154A had no significant effect on clustering (Fig. 3E), and closer inspection of the simulation data revealed an additional salt bridge connecting the F1 loop residue E155 with the αIIb integrin residue R997 in three out of four simulations (charged group distance 3.8±0.8 Å, n=3 simulations), suggesting that either of the D154 and E155 residues might interact with αIIb integrin (Fig. 3D). Indeed, although a single E155A mutation had no effect on clustering,

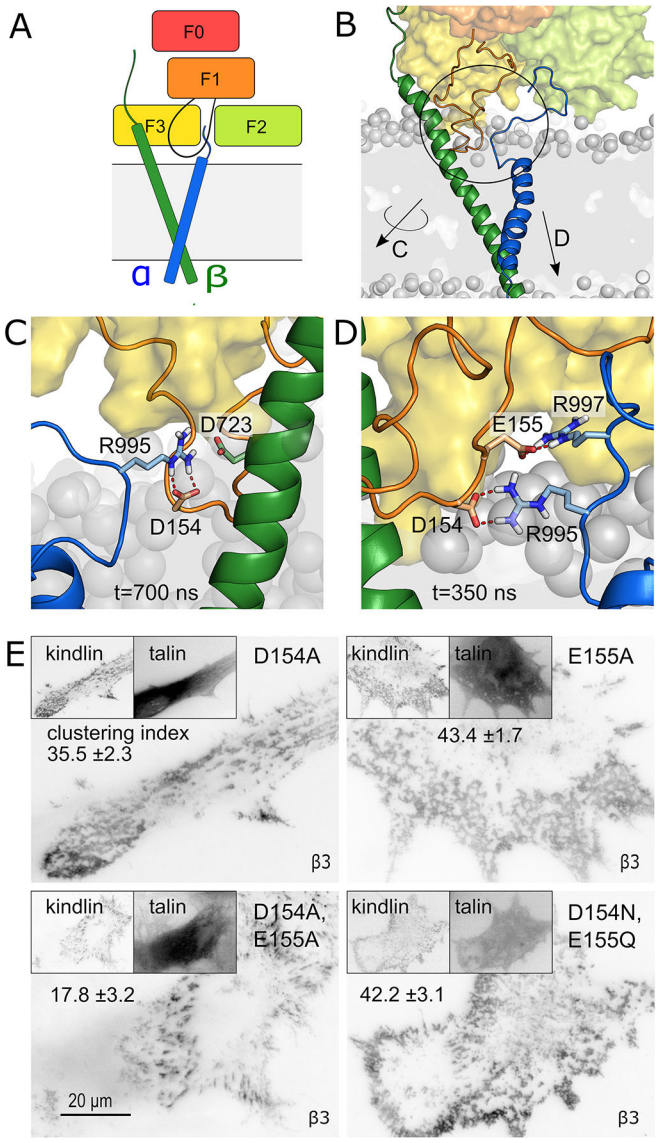

Fig. 3. The F1 loop residues D154 and E155 are critical for β3–GFP integrin clustering. The position of the F1 loop, α- and β-integrin subunits are shown in a schematic manner (A) and in an MD simulation (B). The circled region is shown expanded in C and D (arrows). (C) The D154 residue in the F1 loop interfered with the R995–D723 salt bridge of the integrin αIIbβ3 dimer at the cytoplasm–membrane border in all MD simulations, and a stable salt bridge between talin F1 loop and αIIb R995 was formed. The image is a snapshot from the PIP-B simulation (nomenclature explained in Table S3) at t=700 ns. (D) Salt bridge formation between F1 loop residue E155 and αIIb integrin R997 was observed in three simulations. The image is a snapshot from the no-PIP-B simulation at t=350 ns. (E) Representative TIRF (kindlin-1, β3 integrin) and epifluorescence (talin) images and mean±s.e.m. β3–GFP integrin clustering indices for cells expressing the indicated mutant variants of the talin head domain. Statistical significance was assessed using a one-way ANOVA [$F(4,19)=9.258$, $P=0.0003$] and Tukey's multiple comparison test. Integrin clustering efficiency was significantly compromised in cells expressing t1–435(D154A,E155A) compared to cells expressing wild-type t1–435 talin head ($P<0.001$), whereas the other mutants did not significantly differ from t1–435. The numbers of experiments analyzed were: t1–435, n=10; t1–435(D154A), n=3; t1–435(E155A), n=4; t1–435 (D154A,E155A), n=4; and t1–435 (D154N,E155Q), n=3; 15–25 cells analyzed per experiment. Scale bar: 20 µm.

replacement of both D154 and E155 with alanine residues was as harmful to integrin clustering as the complete deletion of the F0–F1 subdomains. In contrast, replacement with asparagine and

Journal of Cell Science (2020) 133, jcs239202. doi:10.1242/jcs.239202

glutamine (D154N, E155Q) preserved wild-type-like integrin clustering (Fig. 3E).

A previous report has shown that the combined charge inversion of adjacent R153E and K156E residues, as well as that of R146E, prevented lipid interaction of the F1 domain, as well as integrin activation in the context of the talin head domain (Goult et al., 2010). We therefore also tested talin head mutants R153A (LLR^{153}D-LLAD) and L151A, L152A, D154A (LLR^{153}D-AARA), to detect potential interference of integrin clustering. Similarly to the individual D154A mutant, both of these mutants showed normal talin-induced integrin clustering (Fig. S1C), suggesting that membrane binding of the F1 loop is shared by multiple basic residues, as is the potential to activate and cluster integrins by the acidic motif.

Both molecular modeling and integrin clustering assays thus suggested that acidic residues in the F1 loop regulated β3 integrin activation and clustering. To assess whether this regulation takes place via direct interaction of the talin F1 loop with the integrin heterodimer in living cells, we introduced cysteine residues into sites along the inner membrane clasp of β3 integrin and along the mid-part of the F1 loop. We avoided the mutation of residues directly involved in the stabilization of the inner membrane clasp, such as D723 and R995, which might have modified the integrin activation and clustering state independently of kindlin and talin. COS7 cells were transfected with plasmids encoding mouse αv integrin (also known as ITGAV) and human kindlin-1, along with cysteine-mutated talin heads and β3 integrins. To prevent palmitoylation of these newly added cysteines, cells were incubated overnight with bromopalmitate prior to permeabilization with saponin. During saponin permeabilization, cysteine thiol groups were oxidized with copper phenanthroline to promote covalent integrin–talin binding via intermolecular disulfide bonds within integrin–talin complexes persisting in the cells during the permeabilization and oxidation treatment (Fig. 4A). After cell extraction, covalently linked proteins were subsequently identified using non-reduced SDS–PAGE followed by western blotting. Of the five different integrin mutants tested, only the β3(H722C) and β3(I719C) integrin variants yielded covalent heterodimers with the t1–435(L152C) and t1–435(D154C) talin head mutants, representing a restricted subset of the five different F1 loop variants tested (Fig. 4B–E; Fig. S2). In addition, β3(H722C) formed a heterodimer with t1–435(L151C). It is important to note that in the extended talin head conformation (Elliott et al., 2010), the F1 loop and integrin would not reach sufficiently close proximity for disulfide bonding, whereas the FERM-like conformation would enable the observed contacts between the F1 loop and the β3 integrin, and would therefore also explain an interference of the F1 loop with β3 integrin binding to the F3 domain *in vitro* (Table S2).

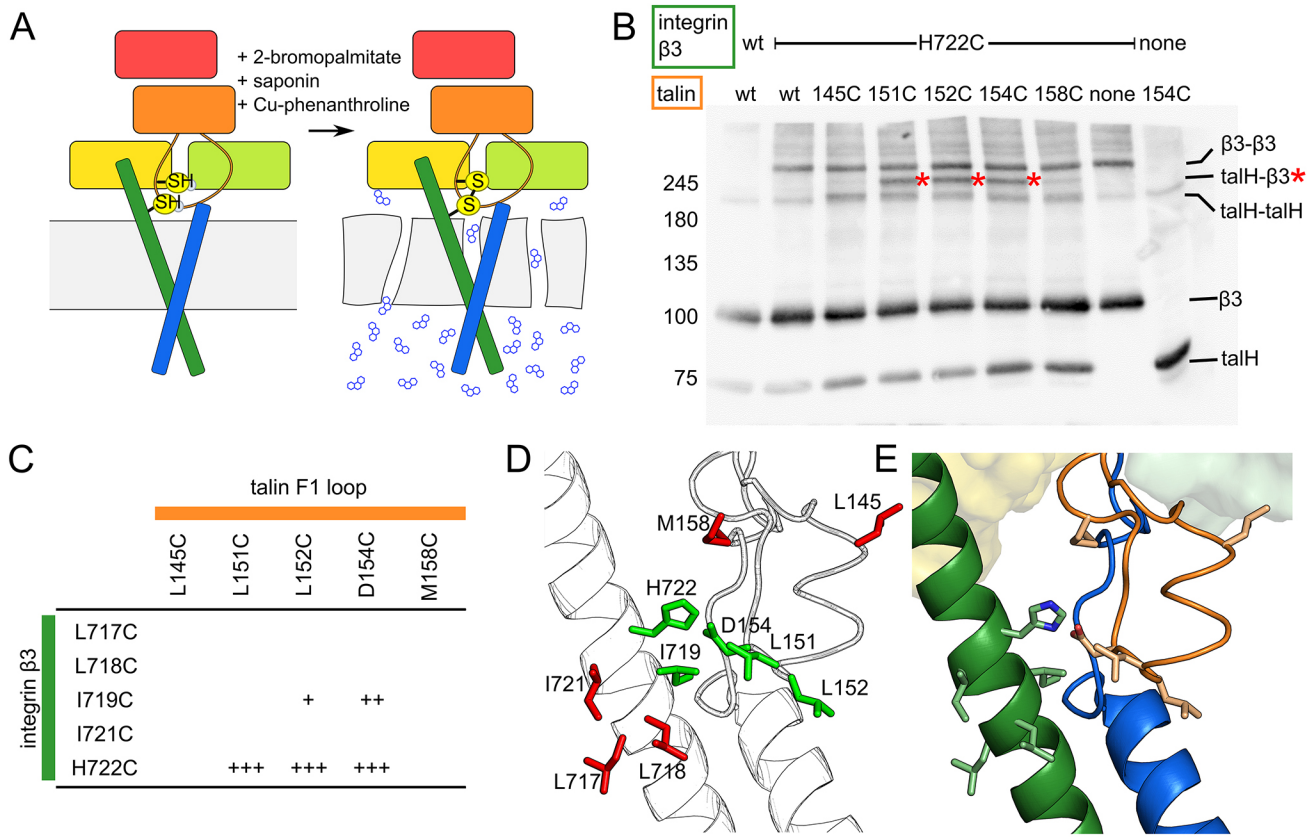

Fig. 4. The F1 loop directly interacts with β3 integrin in COS7 cells. (A) Schematic diagram of the cysteine mapping procedure. Cysteine-mutated CFP–talin head and β3–GFP integrin, as well as RFP–kindlin-1 and unlabeled αv integrin were overexpressed in COS7 cells. The cells were treated with 2-bromopalmitate to prevent cysteine palmitoylation, the membrane was permeabilized with saponin and oxidizing conditions were introduced by treating the cells with phenanthroline, allowing neighboring cysteines in the cytoplasm (above the membrane) to form disulfide bridges. Blue small molecules represent phenanthroline. (B) Representative anti-GFP western blot showing either wild-type (wt) or H722C β3 integrin crosslinking to wt or cysteine-mutated talin heads (talH). Talin–integrin heterodimers in the L151C, L152C and D154C lanes are highlighted with asterisks. (C) Disulfide bonding efficiencies between talin (horizontal) and integrin residues (vertical). (D) The target residues of cysteine mapping in integrin and talin are shown as sticks. Disulfide-bonding residues are shown in green and non-bonding residues in red. (E) Colored representation of D, cysteine-mutated residues from integrin (green) and the F1 loop of talin (orange) are shown as sticks.

Journal of Cell Science (2020) 133, jcs239202. doi:10.1242/jcs.239202

The F1 loop is in contact with the FERM-folded talin head

In order to obtain further insight into the role and position of the F1 loop in the compact FERM-folded talin structure, we closely analyzed the interface between subdomains F2 and F3 (Fig. 5A). In previously published talin head structures that either did not include the F0 and F1 domains (Anthis et al., 2009) or showed the elongated talin head fold (Elliott et al., 2010), the F2–F3 domains are closely associated and linked together by a salt bridge connecting E269 and K345. However, this salt bridge was not present in our FERM-based model, or in the FERM-folded talin head structure (P.Z., L.A., S.K. et al., unpublished). This led to large solvent-exposed surfaces in the model, which were centered around a solvent-exposed Leu314 in the F3 subdomain and Gly226 in the F2 subdomain, forming potential surfaces for interaction with the F1 loop (Fig. 5A). Indeed, observations of our MD simulations suggested stable hydrophobic and charge–charge interactions of C-terminal F1 loop residues with both the F3 (Fig. 5B) and F2 subdomain surfaces (Fig. 5C).

To investigate whether such F1 loop interactions with the F2 and F3 subdomains would be stable, and whether they contribute significantly to domain–domain interactions within the talin head, we applied two mass spectrometry methods to study the compactness and subdomain interactions of the talin head in

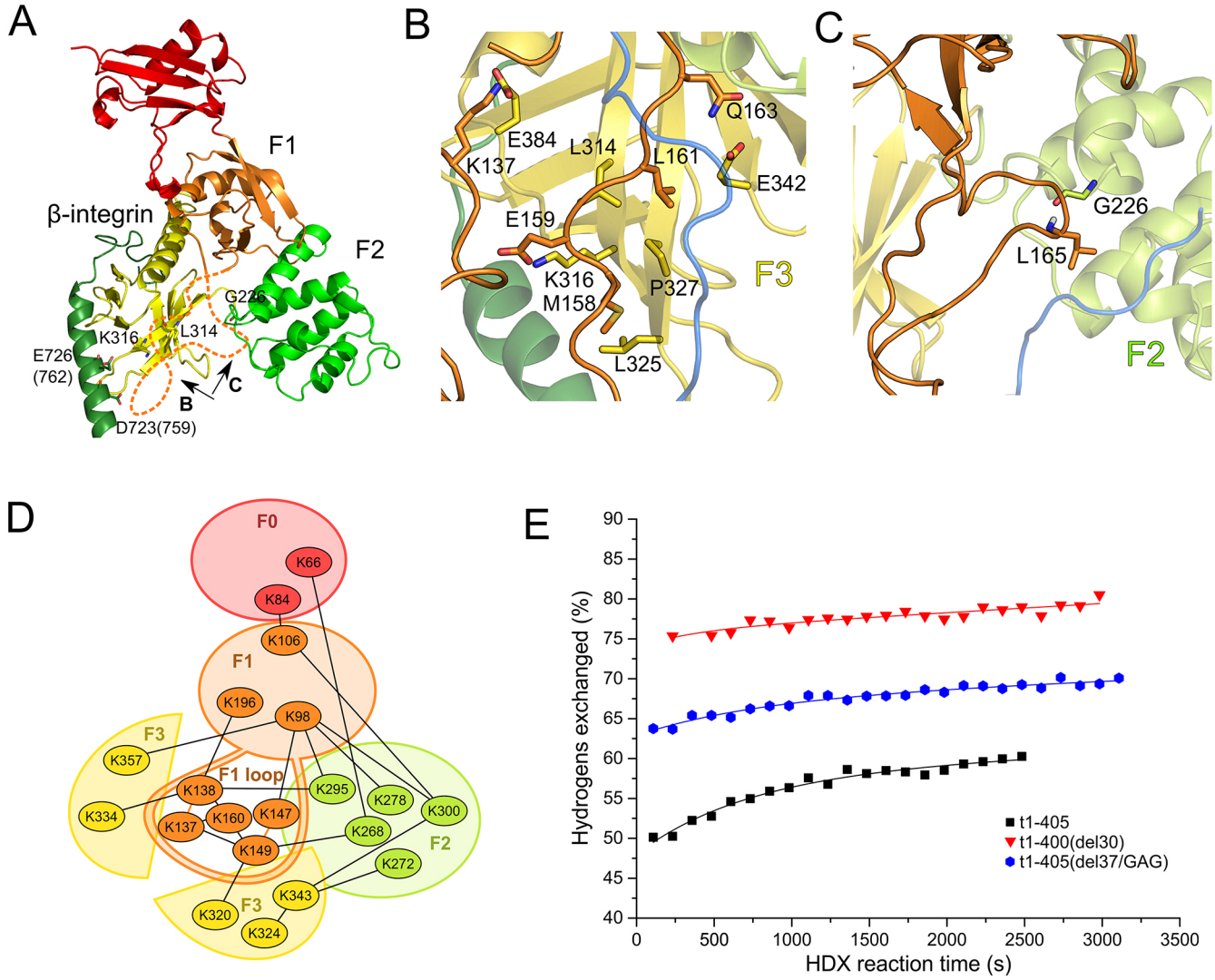

Fig. 5. The F1 loop interacts with F2 and F3 subdomains in the FERM-folded talin head. (A) Overlay of the FERM-folded talin head model with talin-2(F3)–β1D integrin tail (Anthis et al., 2009), fitted at the F3 domain. Please note the gap between F2 and F3 domains with exposed hydrophobic residues such as L314 in F3, or short side chains like G226 in F2 (talin-1 numbering). The missing F1 loop in these structures is indicated by a dotted orange line. Acidic residues in the membrane-proximal domain of β1D integrin known to participate in the inner membrane clasp are numbered as in β3- and β1D-integrins (brackets). Arrows denote regions shown in B and C, as indicated. (B) Interface of F3 with F1 loop from the MD simulation, showing hydrophobic side-chain matching and reciprocal charge distributions. (C) View of the F2–F1 loop interface with anchored L165 sidechain in the F2 subdomain. Please note the trace of the α integrin cytoplasmic tail in blue. (D) Lysine–lysine crosslinking of talin head t1–405. Disuccinimidyl suberate crosslinking followed by trypsin treatment and mass spectrometry analysis showed short distance (linker length ∼1 nm) interactions within the talin head subdomains and F1 loop. The crosslinks are shown as black lines. The proximity of residues K137 and K138, and K147 and K149, in the F1 loop is highlighted with orange lines. Only a single molecular weight was detected for each crosslink, except K272–K343, which was identified via two different peptides. Please note the crosslinks of K149 from the F1 loop with both the F2 residue K268 and F3 residue K320, demonstrating proximity of the F1 loop to both F2 and F3 subdomains. (E) Hydrogen–deuterium exchange mass spectrometry analysis comparing the solvent accessibility of residues in the intact talin head t1–405 and in two F1 loop-deleted forms, measured as percentage of hydrogens exchanged as a function of time. The red curve shows data for the t1–400(del30) construct, representing the elongated talin head, while the blue curve represents the loop-deleted FERM-folded talin head.

Journal of Cell Science (2020) 133, jcs239202. doi:10.1242/jcs.239202

solution. Firstly, we characterized the inter-subdomain interactions in the talin head by crosslinking lysine residues using disuccinimidyl suberate (DSS). Monomeric talin head was separated from its oligomeric species by electrophoresis, then trypsinized and analyzed by mass spectrometry. The analysis confirmed that the F1 loop readily interacts with the F1, F2 and F3 subdomains (Fig. 5D; Table S4). However, a further classification of the crosslinks was difficult, because the potential flexibility of the F1 loop may dynamically sample the subdomain surfaces to induce multiple crosslinks from one given loop residue. For example, K149, which in our F1 loop model was solvent exposed, formed crosslinks with both K268 from the F2 subdomain and K320 from the F3 subdomain (Fig. 5D; Table S4). The latter crosslink further suggests that the F1 loop can indeed contact regions of the F3 domain that are otherwise relevant for β integrin binding to talin (Anthis et al., 2009) and integrin clustering (Saltel et al., 2009), indicative of a gatekeeper function for the F1 loop.

Secondly, because the crosslinking approach provided limited information about the specific positions of the F1 loop, we analyzed the compactness of three talin head forms using hydrogen–deuterium exchange mass spectrometry (HDX-MS). The HDX-MS profiles of the talin head variants t1–405, t1–400(del30) and t1–405(del37/GAG) showed major differences in their deuterium intake versus exchange time (Fig. 5E). The native form containing an intact F1 loop (t1–405) clearly showed the lowest HDX rate among the talin forms (up to ∼60% in 2500 s), and had a population of very rapidly exchanging (burst phase) hydrogens, which represented labile side-chain or non-hydrogen-bonded, solvent-exposed backbone hydrogens. In addition, ∼40% of all hydrogens in t1–405 were tightly hydrogen bonded or located in the hydrophobic core and were not exchanged within 1 h of reaction time. The HDX rate was, however, clearly faster for the loop-deleted form t1–405(del37/GAG) and even faster for t1–400(del30), which corresponds to the construct that formed the extended talin head structure during crystallization. Thus, the results suggest that the F1 loop is an integral part of the talin head structure, where it covers parts of the F2 and F3 domains. On the other hand, the C-terminal lysines, absent in the tl–400(del30) construct, may connect the F3 and F1 subdomains, thereby stabilizing the compact structure. Whereas the removal of the F1 loop results in new solvent-exposed talin residues, moderately increasing the HDX rates, the additional C-terminal truncation of the talin head (t1–400) induces an open and flexible structure that is reflected by a further considerable increase in HDX rates (Fig. 5E).

Lastly, we studied the t1–405, t1–405(del30) and t1–405(del37/GAG) talin head variants using small-angle X-ray scattering (Fig. S3). Inline size exclusion chromatography was utilized to ensure monodisperse scattering data derived only from monomers. Kratky analysis indicated that all of the talin forms studied were partially flexible, with t1–405(del37/GAG) being slightly more compact than the other forms (Fig. S3E). To account for the apparent flexibility of talin in solution, we analyzed the talin head solution conformation using the Ensemble Optimization Method (Eom) (Tria et al., 2015). In this analysis, the Eom program generated a pool of talin head domain models from the individual subdomain 3D structures (PDB ID 3IVF; Elliott et al., 2010) with the missing F1 loop and linkers *ab initio*-modeled as dummy residues. The program then selected an ensemble of conformations that best fitted the scattering data using a genetic algorithm, and this conformational ensemble was represented by a few conformations. The analysis suggested that most of the talin head molecules in the samples were in a FERM-like conformation (Fig. S3). Moreover, the calculated conformational ensembles of all the talin head forms showed narrow R_g distributions, and again the t1–405(del37/GAG) was observed to be more compact than the other talin head forms or a random pool (Fig. S3). The results thus propose that FERM-shaped talin head folds are the major constituent of the talin samples, irrespective of the presence or absence of the F1 loop.

The F1 loop is critical both in the talin head and in full-length talin

All of our cell biological experiments reported thus far were carried out with the talin head domains in a β3 integrin context. Talin head alone does not become autoinhibited and, hence, is more potent in integrin activation and clustering than full-length talin (Goksoy et al., 2008; Saltel et al., 2009). However, the head domain alone is not properly coupled to the cytoskeleton (Cluzel et al., 2005), because two of the three actin-binding sites in the talin protein are located in the rod domain (Hemmings et al., 1996). To analyze the function of the F1 loop within the complete protein, we expressed wild-type (t1–2541), loop-deleted [t1–2541(del37/GAG)] and point-mutated talins in talin-1$^{-/-}$ talin-2$^{-/-}$ mouse kidney fibroblast cells (Theodosiou et al., 2016) and detected the extended and activated forms of β1 integrin by FACS using the conformation-specific 9EG7 monoclonal antibody. Whereas no 9EG7 staining was detected on talin-null cells, the expression of wild-type talin t1–2541 protein rescued the 9EG7 staining to levels comparable to those in talin-floxed cells (data not shown). The loop-deleted talin t1–2541(del37/GAG) only partially activated β1 integrins, comparable to the effects of an R358A talin mutant [t1–2541(R358A)], which reportedly reduces β3 integrin binding (García-Alvarez et al., 2003). The loop deletion was, however, less harmful to integrin activation than the membrane-proximal β integrin binding site mutant t1–2541(K316E,K324E) (Saltel et al., 2009) (Fig. 6A). Furthermore, the previously proposed phosphomimetic F1 loop mutant t1–2541(T144E,T150E) activated β1 integrin less efficiently than wild-type t1–2541, which is also consistent with the reduced β3 integrin binding of a talin head construct of this mutant *in vitro* (Table S2). In contrast, the phosphorylation-deficient variant t1–2541(T144A,T150A) behaved like wild-type talin in the β1 integrin activation assay (Fig. 6A), and showed kindlin-1-independent integrin clustering in B16F1 cells (Fig. S1D). This suggests that the loop structure and integrin activation function is modulated by phosphorylation at these residues.

Thus, the loop deletion in full-length talin impaired the activation of β1 integrin in suspended cells. Although the 'inside-out' activation by loop-deleted talin works poorly in this situation, tension from integrin attachment to a rigid fibronectin-coated surface may still provide 'outside-in' activation of integrins, leading to integrin clustering and cell spreading. Indeed, on a rigid and saturated fibronectin substrate, besides a reduction in cell spreading area, talin-knockout cells expressing wild-type or F1 loop-deleted talin (t1–2541) constructs spread comparably (data not shown).

To explore cell spreading in a more natural setting, we used cell-derived 3D fibronectin-containing matrices. After an incubation of 6 h, cells expressing loop-deleted talin had an area of 870±335 μm^2 (mean±s.d.), whereas cells expressing the intact talin form had spread out to an area of 1359±503 μm^2 (Fig. 6B,C). Intriguingly, cells expressing wild-type talin formed longer 'fibrillar-like' adhesions, whereas in cells transfected with loop-deleted t1–2541(del37/GAG) talin, adhesions were shorter (Fig. 6D). Thus, β1 integrin activation was partially inhibited by the loop deletion, affecting cell spreading in complex 3D matrices and the elongation of adhesions along 3D extracellular matrix fibrils.

Journal of Cell Science (2020) 133, jcs239202. doi:10.1242/jcs.239202

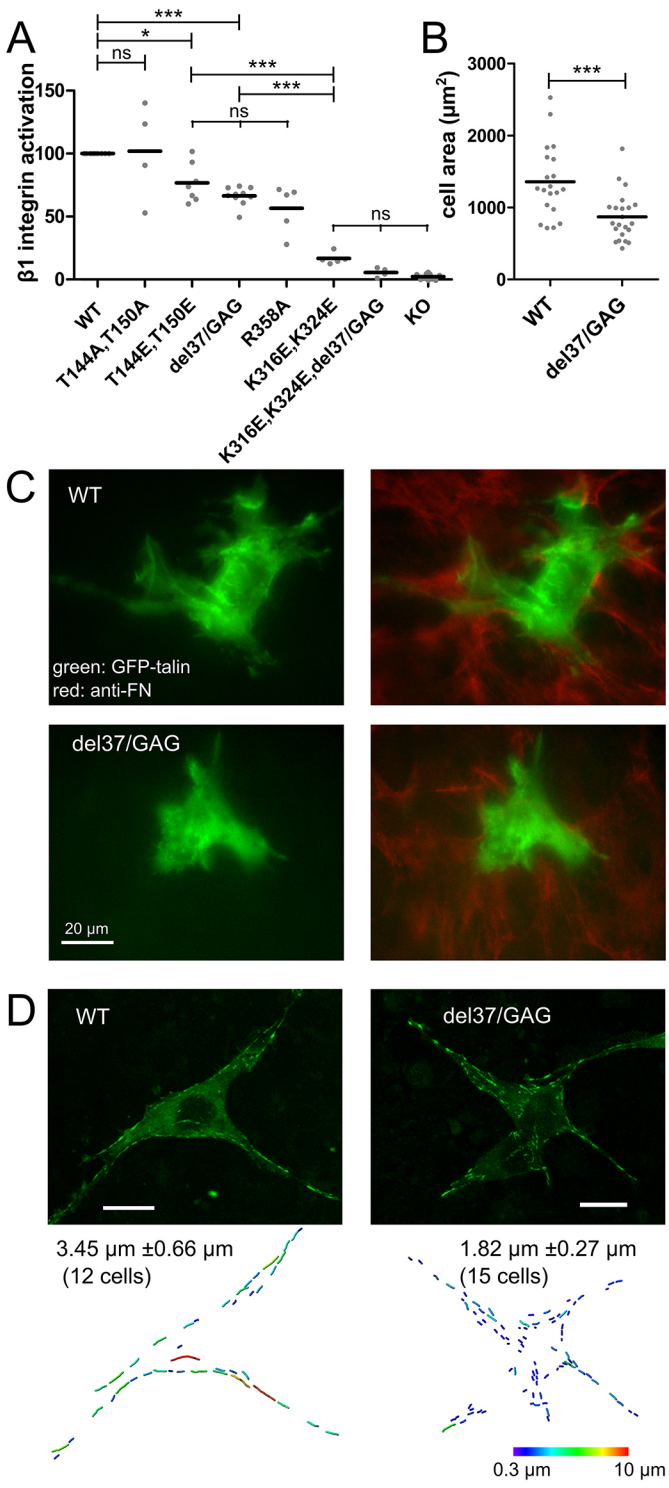

Fig. 6. F1 loop-deleted full-length talin rescues integrin activation in talin-knockout cells, but both integrin activation and adhesion maturation are impaired. (A) Activation of β1 integrin by wild-type (WT) and F1 loop-deleted full-length talin. Talin knockout cells (KO, *n*=10), and cells expressing talin constructs with an N-terminal GFP tag (WT, *n*=10; del37/GAG, *n*=10; T144E T150E, *n*=7; T144A T150A, *n*=4; R358A, *n*=5; K316E K324E, *n*=5; and K316E K324E+del37/GAG, *n*=4). The activation indices were normalized to GFP-tagged wild-type talin. Normalized activation indices are shown as points, with the mean indicated by a line. Statistical analysis was carried out using a one-way ANOVA [$F(7,47)=66.13$, $P<0.0001$] and Tukey's multiple comparison test. (B) Spreading of talin-knockout cells expressing the wild-type (*n*=42 cells) and F1 loop-deleted (*n*=30) full-length talin on a 3D matrix. Cell area was measured at 6 h. Lines indicate the mean values. Statistical analysis was carried out using an unpaired two-tailed *t*-test [$t(40)=3.740$, $P=0.0006$]. (C) Cell spreading and fibronectin remodeling in 3D culture. Representative talin-knockout cells expressing the indicated talin variants are shown. Red, anti-fibronectin; green, GFP–talin. (D) Top: two representative talin-knockout cells expressing the wild-type and loop-deleted GFP-labeled full-length talins are shown. Green, GFP–talin. Bottom: average single adhesion lengths (mean±s.e.m.) of the indicated number of cells, along with individual adhesions for the representative cells, color-coded by length of adhesions as determined using the Imaris software (Bitplane, Zürich, Switzerland). Scale bars: 20 μm. $^{*}P\leq0.05$; $^{***}P\leq0.001$; ns, not significant.

DISCUSSION

Talin plays a key role in integrin-mediated cell–matrix interactions. The function of the F1 loop in the talin head domain has been found important in previous studies, where it was proposed that it either worked through a fly-cast mechanism (Goult et al., 2010) or by continuing the lipid-binding ridge of the F3 and F2 subdomains towards the N-terminal part of an extended form of the talin head domain (Kalli et al., 2013). The reduction of integrin activation and clustering by phosphorylation of F1 loop residues (Fig. 6; Goult et al., 2010) may indeed suggest that differential membrane interaction of the F1 loop controls integrin function. Similarly the loss of kindlin-mediated control of integrin clustering by T144A/T150A substitutions in the F1 loop (Fig. S1D) is consistent with altered muscle attachment site remodeling observed for a T152A mutant in *Drosophila* (Katzemich et al., 2019), and may also indicate a link between kindlin and the phosphorylation state of the F1 loop. However, independent of the regulation of the talin–membrane interaction, the identification of conserved acidic residues critical for integrin activation and clustering that are localized immediately adjacent to the inner membrane clasp reveals a much more direct way of controlling integrin activation and clustering than by differential membrane recruitment of the talin head.

The crosslinking and SAXS data suggest that the head domain of talin assumes a compact FERM fold, which positions the talin F1 loop next to the integrin-binding site in the F3 subdomain of talin (K316, K324 and L325; see Fig. 5B). This site in talin interacts with the membrane proximal acidic (Saltel et al., 2009) and hydrophobic (Wegener et al., 2007) integrin-activity regulating motif D^{723}R[K/R]EFAKF to take a central role in the β1- and β3-integrin activation and clustering process regulated by talin and kindlin. Selected acidic residues of the F1 loop appear to target the positively charged juxtamembrane residues in the integrin α subunit thereby interfering with the inner membrane clasp and inhibiting α–β subunit association in order to stabilize the extended conformation of the integrin. The recently reported binding of the Rap1 adaptor to the talin F1 or F0 subdomains (Zhu et al., 2017; Bromberger et al., 2018; Lagarrigue et al., 2018; Gingras et al., 2019) might, in turn, help to stabilize the orientation and membrane tethering of the FERM-folded talin head in order to strategically position the F1 loop and to regulate integrin activation in an F1 loop-dependent manner (Gingras et al., 2019).

While talin and kindlin binding to integrins rearranges the integrin juxtamembrane- and ecto-domains, talin itself is also regulated through conformational changes (Goksoy et al., 2008; Song et al., 2012; Goult et al., 2013; Ye et al., 2016). Our results suggest that additional subtle regulations of the talin–integrin interface may take place within the talin head. The deletion of either the entire F0–F1 subdomains or only the F1 loop enhanced talin

Journal of Cell Science (2020) 133, jcs239202. doi:10.1242/jcs.239202

head binding to wild-type β3 integrin, whereas phosphomimetic mutations (T144E, T150E) in the F1 loop reduced this binding (Table S2), suggesting that the phosphorylation of the F1 loop can regulate β3–F3 interactions. Accordingly, the phosphomimetic T144E, T150E mutations impaired β1 integrin activation by full-length talin (Fig. 6A) and β3 integrin clustering by the talin head (Fig. S1D). Moreover, the mutagenesis of T144 and T150 (T144A, T150A) enhanced integrin clustering independent of additional kindlin-1 expression. In contrast, both the neutral F1 loop mutant (151–154AAAA) and the mutant with increased net charge (D154A, E155A) clustered integrin poorly (Figs 2F,G and 3E), suggesting that the F1 loop has functions beyond charge interactions with membrane lipids. We observed that the L152 residue of the LLRD151–154 region can stretch and enter into the hydrophobic core of the membrane in all talin–integrin–lipid simulations (Fig. S1A). The LLRD stretch may thus help to guide the D154 or E155 residues to membranes and even to interact directly with integrin at the level of the inner membrane clasp (Fig. 4). The F1 subdomain, and the F1 loop in particular, may therefore function as a gatekeeper in raising the threshold for initial talin–integrin association, while promoting the stability of the unclasped, activated form of the bound integrin heterodimers.

This model is particularly interesting in the light of mechanical tension exerted on the integrin bond. When the talin head induces integrin activation and clustering in a low-force regime, the presence of the F1 loop is required for maintaining the conformational changes of cell-surface-exposed integrins for rapid binding of soluble ligands (inside-out activation). In contrast, when integrins are exposed to mechanical forces, such as those encountered within a rigid 3D matrix scaffold, the integrin catch bond is able to maintain the extracellular domain in a ligand-bound conformation, reducing the requirement for the F1 loop to keep the integrin activated. Therefore, the equilibrium between different integrin conformations at the cell surface, and their functional roles, could be regulated by the F1 loop and the affinity of the talin head for the integrin. Thus, the different types of ECM adhesion and differential remodeling capacity of the extracellular matrix, as recently shown for the β1A- and β1D-integrin splice variants (Soto-Ribeiro et al., 2019), could be explained by different affinities for the talin head domain (Anthis et al., 2010) as well as changes in integrin signaling capacities that potentially affect talin F1 loop residues (Katzemich et al., 2019).

In conclusion, structural and mutational analysis shows that the conformation of the talin head in solution adopts the shape of a FERM domain. In cells, the talin F1 loop directly interacts with residues of the inner membrane clasp of integrins, enabled by the specific projection of the F1 loop from a compact FERM-folded talin head. The FERM configuration of talin provides a scaffold that allows the docking of upstream integrin regulators such as Rap1, in order to position the F1 loop for the talin-dependent regulation of β integrin activation and clustering (Fig. S4). This integrin activation process is assisted by a kindlin-dependent mechanism that leads to integrin clustering, which is required for efficient linkage of integrins to the actin cytoskeleton, and by regulation of integrin signaling, which in turn can be modulated by the phosphorylation state of the F1 loop of talin.

MATERIALS AND METHODS

Protein production

Talin head domains (Table S1) were expressed using the pTrcHis C vector (Thermo Fisher Scientific, Carlsbad, CA), which includes an N-terminal hexahistidine tag (MGGSHHHHHHGMASMTGGQQMGRDLYDDDDKDRWIRPRA). The sequence-confirmed plasmids were introduced into *E. coli* BL21-Star cells (Thermo Fisher Scientific). Bacteria were cultured in LB medium containing 100 µg/ml of ampicillin at 37°C. IPTG (1 mM) was used to induce protein expression at an optical density of 0.4, and cells were harvested after 5 h of incubation. *E. coli* extracts were prepared by homogenization (Emulsiflex C3) in 20 mM $NaPO_4$ pH 7.4, 1 M NaCl and 20 mM imidazole. Clarified lysates were applied to a HisTrap FF 5 ml affinity column (GE Healthcare) using an ÄKTA purifier (GE Healthcare). Talin head domains were eluted from columns using 20 mM sodium phosphate buffer pH 7.4 containing 1 M NaCl with gradually increasing imidazole concentration (20–700 mM). Eluted fractions were analyzed by SDS–PAGE and Coomassie staining and were pooled when appropriate. Furthermore, talin head domains were purified using a HiTrap SP FF 1 ml column (GE Healthcare) after dilution (1:10) in 50 mM $NaPO_4$, 20 mM NaCl, pH 7.2 buffer. Elution was performed by preparing a linear NaCl gradient with 50 mM $NaPO_4$, 1 M NaCl pH 7.2 buffer.

GST–β3-integrin-tail fusion constructs (WT-beta3, GST–GSKLLITIH-DRKEFAKFEEERARAKWDTANNPLYKEATSTFTNITYRGT; and beta3-VE, GST–GSKLLITIHDRKEFAKFEEERARAKWVENPLYKEA-TSTFTNITYRGT) were expressed in *E. coli* BL21-Star cells using a similar approach. Cells were lysed by homogenization (Emulsiflex C3) in phosphate-buffered saline (PBS) pH 7.4 buffer, and proteins were purified with Glutathione Sepharose (GE Healthcare 4 Fast Flow) using buffer containing 50 mM Tris-HCl pH 8 and 20 mM reduced glutathione as eluent. Eluted fractions were analyzed with SDS–PAGE, Coomassie staining, and western blotting using mouse anti-GST B-14 (Santa Cruz) and goat anti-mouse antibodies. Fractions containing the desired proteins were dialyzed into 50 mM sodium phosphate buffer, pH 7.2, containing 150 mM NaCl and stored at −20°C.

The homogeneity of the purified proteins was evaluated using dynamic light scattering (Malvern Zetasizer ZS). The purified talin proteins were also subjected to high-resolution mass spectrometric analysis. The mass spectra indicated that the protein samples were pure and homogeneous, and the determined accurate masses were in a full agreement with those calculated from the sequences.

Mass spectrometry

Talin head molecular weight determination and hydrogen–deuterium exchange mass spectrometry experiments were performed on a Bruker Apex-Qe FT-ICR instrument (Bruker Daltonics, Billerica, MA), equipped with an Apollo-II ESI source and an actively shielded 12-T superconducting magnet. First, all talin samples were buffer exchanged into 200 mM ammonium acetate (pH 7) using Sephadex G-25 columns (PD-10; GE Healthcare Life Sciences). The protein concentrations were determined by absorbance at 280 nm using sequence-derived extinction coefficients. The samples were further diluted with acetonitrile:water (50:50 v/v) containing 1% acetic acid to a final concentration of 1–10 µM. The produced protein ions were accumulated in the collision cell for 100 ms and transferred to the Infinity ICR cell for trapping, broadband (*m/z* 500–3000) excitation and detection. For each spectrum, a total of 200 time-domain transients (1 MWord) were co-added. All mass spectra were externally calibrated by using ESI-L Tuning Mix calibration mixture (Agilent Technologies). The spectral acquisition and data post-processing were accomplished using Bruker DataAnalysis 4.4 software. Neutral, most abundant protein masses were obtained through a standard charge deconvolution and compared to those calculated from the protein sequences (Table S1).

Hydrogen–deuterium exchange

In hydrogen–deuterium exchange mass spectrometry (HDX-MS) experiments, all talin samples were first buffer-exchanged to 200 mM ammonium acetate (pH 7) by using Sephadex G-25 columns (PD-10; GE Healthcare Life Sciences). The protein concentrations were determined by absorbance at 280 nm using sequence-derived extinction coefficients. The determined protein concentrations varied between 5 and 50 µM. Native HDX-MS measurements were subsequently performed by diluting 40 µl of each protein stock solution with 160 µl of D_2O (99.9% D) to initiate HDX. Therefore, the maximum theoretical deuterium intake was 80%. In order to obtain sufficient spectral intensities for the least concentrated talin samples,

greater dilution factors could not be used. After mixing, the samples were immediately delivered to a 250 µl Hamilton glass syringe and continuously infused (1.5 µl/min) to the ESI source using a syringe pump. The ESI-generated ions were accumulated in the collision cell and transferred to the Infinity ICR cell for trapping, broadband (*m/z* 1000–5000) excitation and detection. All ion source and ion transmission parameters were optimized for native MS experiments. The HDX mass spectra were measured in an automated fashion by 125-s intervals (the first spectrum was acquired after a period of 107.5 s to ensure that the spray current had been stabilized) up to ∼1 h. For each spectrum, a total of 40 time-domain transients were co-added and fast-Fourier transformed prior to magnitude calculation. Each recorded transient had only a 128-kWord data size (equal to the transient length of ∼0.11 s) to increase the time-resolution of the experiments (at the expense of spectral resolution). The final transformed data were downsampled to 32 kWord using Gaussian multiplication to improve peak shapes and allow straightforward peak centroid location, and finally charge deconvoluted. The control experiments (0% D) were performed by diluting the protein samples with H_2O instead; these experiments were performed with two different time-domain data sizes (128 and 1024 kWord), the latter providing isotopically resolved spectra for a more accurate molecular mass determination. All mass spectra were externally calibrated by using ESI-L Tuning Mix calibration mixture (Agilent Technologies). The spectral acquisition and data processing was accomplished using Bruker XMASS 7.0.8 software.

The data analysis for HDX-MS experiments was as follows. The maximum theoretical number of exchangeable hydrogens (D_{max}) in each protein construct was calculated as: $D_{max}=3n_{Arg}+2n_{Lys}+2n_{Gln}+2n_{Asn}+n_{His}+n_{Ser}+n_{Thr}+n_{Cys(SH)}+n_{Tyr}+n_{Asp}+n_{Glu}+n_{total}+n_{charge}-n_{Pro}-1$, where n_{Xxx} is the number of the respective residue in the sequence, n_{total} is the total number of residues (counting for backbone amide hydrogens) and n_{charge} is the average number of charges in the observed protein ions. The relative deuterium intake (% *D*) at each time point was calculated as $\%\ D=(m_D-m_H)/(0.80\times D_{max})$, where m_D and m_H are the masses of the deuterated and undeuterated protein samples, respectively. For each time point, the HDX reaction time (t_{react}) was calculated as $t_{react}=(t_{start}-t_{end})/2$, in which t_{start} and t_{end} are the starting and ending time points of the spectral acquisition. This calculation assumes roughly linear deuterium intake for the given time window. Finally, % *D* was plotted against t_{react}, and the data were fitted with a kinetic model of three exponential terms, representing fast, slow and very slow exchanging hydrogens. The fitting was accomplished using OriginPro 15 software (OriginLab Corporation).

Disuccinimidyl suberate crosslinking

A talin head sample (t1–405, 1 mg ml^{-1} in $NaPO_4$ pH 7.2 and 150 mM NaCl) was crosslinked with 50× molar excess of disuccinimidyl suberate (DSS) according to the manufacturer's instructions (Thermo Fisher Scientific). The crosslinked talin particles were separated by electrophoresis on a Bolt 4–12% Bis-Tris Plus gel (Thermo Fisher Scientific). The ∼50 kDa bands were excised, and peptides were extracted from the gel slices by in-gel digestion according to methods previously described (O'Connell and Stults, 1997). Cysteine bonds were reduced with 0.045 M dithiothreitol (DTT; D0632 Sigma-Aldrich) for 20 min at 37°C, followed by alkylation with 10 mM iodoacetamide (57670 Fluka, Sigma-Aldrich) at room temperature. The proteins were then digested to peptides using sequencing-grade modified trypsin (V5113, Promega) at 37°C overnight. After quenching with 10% trifluoroacetic acid (TFA), the peptides were desalted by C18 reversed-phase spin columns according to the manufacturer's instructions (Harvard Apparatus). The eluted peptide sample was dried in vacuum centrifuge and reconstituted to a final volume of 30 µl buffer containing 0.1% TFA in 1% acetonitrile (ACN).

Liquid chromatography–mass spectrometry (LC-MS) analysis was performed on an EASY-nLC 1000 system (Thermo Fisher Scientific) connected to a Q-Exactive mass spectrometer (Thermo Fisher Scientific) with nano electrospray ionization sprayer (Thermo Fisher Scientific). In detail, peptides were eluted and separated with a C18 pre-column (Acclaim PepMap 100, 75 µm×2 cm, 3 µm, 100 Å; Thermo Fisher Scientific) and analytical column (Acclaim PepMap RSLC, 50 µm×15 cm, 2 µm, 100 Å; Thermo Fisher Scientific), using a 60 min buffer gradient ranging from 5 to 35% buffer B, followed by a 5 min gradient from 35 to 80% buffer B and 10 min gradient from 80 to 100% buffer B at a flow rate of 300 nl/min (buffer A: 0.1% formic acid in 98% HPLC grade water and 2% ACN; buffer B: 0.1% formic acid in 98% ACN and 2% water). For direct LC-MS analysis, 4 µl peptide sample was injected to the LC-MS/MS and analyzed. Data-dependent FTMS acquisition was in positive ion mode for 80 min. A full scan (200–2000 *m/z*) was performed with a resolution of 70,000, followed by top10 CID-MS2 ion trap scans with resolution of 17,500. Dynamic exclusion was set for 30 s.

The search engine pLink (v2.3.3; http://pfind.ict.ac.cn/software/pLink) (Lu et al., 2015) was used to identify the intra-protein crosslinked peptides. The precursor mass tolerance was set at 10 ppm and 0.05 Da for the fragment mass tolerance, and the FDR was set to <1% at spectral level. All spectra of putative crosslinked peptides were manually controlled before positive identification. The extended and FERM conformations were compared in terms of inter-residue distances of the identified crosslinks using MNXL analysis (Bullock et al., 2016).

Analytical light scattering

Proteins were analyzed using a liquid chromatography instrument (CBM-20A, Shimadzu Corporation, Kyoto, Japan) equipped with an autosampler (SIL-20A), UV-VIS (SPD-20A) and a fluorescence detector (RF-20Axs). Molecular weight was determined using size-exclusion chromatography with a Malvern Zetasizer µV instrument (Malvern Instruments Ltd, Worcestershire, UK) measuring inline Static Light Scattering (SLS) and Dynamic Light Scattering (DLS). Data were processed using Lab Solution Version 5.51 (Shimadzu Corporation) and OmniSec 4.7 (Malvern Instruments Ltd) software. Samples (50 µg) were injected into the column (Superdex 200 Increase 5/150, GE Healthcare, Uppsala, Sweden) using the autosampler. The column was equilibrated with 50 mM Na_3PO_4 pH 7.2, 150 mM NaCl running buffer. The measurements were run with a flow rate of 0.1 ml/min at 20°C. BSA was used for calibration of the system to calculate molecular weight from the measured SLS intensity.

Differential scanning calorimetry

Talin samples were analyzed using the VP-DSC instrument (MicroCal, Malvern Instruments Ltd) with protein concentrations of ∼0.2 mg/ml in 50 mM NaH_2PO_4 pH 7.2, 150 mM NaCl containing 1 mM EDTA and 1 mM DTT. Concentrations were measured before the analysis by NanoDrop using a theoretical molar extinction coefficient calculated using ProtParam software. Samples were stored at 4°C prior to analysis. Solutions were degassed prior to measurements. Samples were heated from 20°C to 130°C at a scanning rate of 2°C/min. Feedback mode was set to low, and the filter period was 5 s. Temperature transition midpoint (T_m) and calorimetric heat change (ΔH) were obtained by subtracting the baseline and applying the Levenberg–Marquardt non-linear least-squares method to the data using MicroCal Origin 7.0 software (MicroCal, Malvern Instruments Ltd).

Biosensor analysis of talin–integrin interactions

Biosensor analysis was carried out on a ForteBio Octet RED384 instrument (Pall Life Sciences) using Ni-NTA sensors following a strategy similar to the one described by Pinon et al. (2014). Samples or buffers were prepared into 96- or 384-well plates at a volume of 200 µl or 80 µl per well, respectively. Sensors were pre-wetted with buffer (50 mM Na_3PO_4 pH 7.2, 150 mM NaCl) in order to obtain baseline measurements prior to protein immobilization. An operating temperature of 27°C and a stirring speed of 1000 rpm were used throughout the experiment. Sensors were chemically activated by immersion in 0.05 M EDC [1-Ethyl-3-(3-dimethylaminopropyl)carbodiimide] and 0.1 M NHS (*N*-Hydroxysuccinimide) in water for 100 s. Different talin head mutant samples (50 µg/ml) were immobilized on the sensor's surface for 300 s. The excess sulfo-NHS esters were quenched by 1 M ethanolamine pH 8.5 for 100 s. Serially diluted GST–β3-integrin-tail fusion proteins were applied on the talin-coated sensors in concentrations of 20, 80, 320, 1250 and 5000 nM to obtain the relative affinity of talin to GST–β3. Each concentration of GST–β3-integrin-tail fusion protein binding to the sensor was measured for 300 s before moving on to a higher concentration.

Journal of Cell Science (2020) 133, jcs239202. doi:10.1242/jcs.239202

Talin–wild-type β3 integrin (WT-β3) and talin–high-affinity β3 integrin (VE-β3) binding data from Octet biosensor (20, 80, 320, 1250, and 5000 nM) were treated as follows: background (GST control) was subtracted, and all the data were normalized to t1–405 at concentration 1250 nM to allow comparison between experiments. The normalized data were analyzed by linear regression analysis in GraphPad Prism 5.02 (GraphPad Software, La Jolla, CA), assuming one-site specific binding. Bmax was set to 8.6 for WT-β3 binding data and to 1.265 for VE-β3 binding data.

Protein modeling and molecular dynamics

Integrin-αIIb (residues 955–1008) and -β3 (residues 684–762) were modeled as described by Orłowski et al. (2015). A FERM-like fold for the talin head domain was generated using the experimental structures of talin F0, F1, F2, and F3 subdomains [PDB IDs 3IVF (Elliott et al., 2010), 2KC2, 2KMA (Goult et al., 2010) and 2H7E (Wegener et al., 2007)]. The F1, F2 and F3 subdomains were arranged into a FERM-like fold using merlin as a template (PDB ID 1H4R; Kang et al., 2002). The model was prepared in an iterative process of homology modeling, manual adjusting of contacts, energy minimizations and short molecular dynamics simulations (up to 23 ns). The loop missing from the crystallographic structure of talin head, residues 139–168, was added to the FERM fold by selecting the least clashing conformer from the NMR structure of talin F1 subdomain (PDB ID 2KC2; conformer 8). Modeling of the integrin dimer has been described previously (Orłowski et al., 2015). MODELLER (Šali and Blundell, 1993) was used for protein modeling. Quality assessment of the talin–integrin complex used for the molecular dynamics simulations with MolProbity (Chen et al., 2010) gave a MolProbity score of 1.71 (89th percentile) and a clash score of 0.61 (99th percentile).

Molecular dynamics simulations were run at 310 K using Gromacs 4.5.5 (Van Der Spoel et al., 2005) and the OPLS force field (Jorgensen et al., 1996) in 0.15 M KCl and TIP3P water using a setup described previously (Orłowski et al., 2015). The simulated systems are described in Table S3. The resulting MD data has been deposited into IDA research data storage and can be accessed via https://ida.fairdata.fi/s/NOT_FOR_PUBLICATION_AfayjpjdWxyL.

Cell lines

Mouse melanoma B16F1 cells (initially obtained from Garth L. Nicolson, Texas M.D. Anderson Cancer Center, Houston, TX) (Ballestrem et al., 1996) and COS7 cells (ATCC CRL-1651) were cultured in DMEM, 10% fetal calf serum (FCS) and antibiotics and passaged by trypsin treatment as described previously (Cluzel et al., 2005). Talin-1$^{-/-}$ talin-2$^{-/-}$ cells were obtained from Reinhard Fässler, Max Planck Institute of Biochemistry, Martinsried, Germany (Theodosiou et al., 2016), and cultured in DMEM, containing 10% FCS and antibiotics. At each passage, substrate-adhering cells were detached with trypsin treatment and combined with suspended cells, prior to dilution and resuspension in new culture medium.

DNA constructs

Wild-type and mutant human talin1 head domain constructs used for mammalian cell transfection were cloned in pcDNA3 [Invitrogen (Thermo Fischer V79020)] as N-terminal cyan fluorescent protein (CFP) fusion proteins, following standard molecular biology protocols, and confirmed by automated DNA sequencing (Saltel et al., 2009). His-tagged human talin1 head domain constructs were cloned into pTrcHis C vector. GFP-tagged talin1 full-length constructs were cloned into pcDNA3 as an N-terminal tagged human–mouse chimera comprising the human head domain (Saltel et al., 2009) and the mouse rod domain (kindly provided by Anna Huttenlocher, University of Wisconsin–Madison, WI). N-terminal TagRFP-labeled human kindlin-1 (kindly provided by Drs Hongquan Zhang and Staffan Strömblad, Karolinska Institutet, Sweden) was cloned into pcDNA3. Wild-type and VE-mutant forms of the GST–β3-integrin cytoplasmic tail constructs have been described previously (Pinon et al., 2014). C-terminal GFP-tagged mouse β3 integrin constructs were cloned in pcDNA3 and the linker region modified by two additional amino acids, in comparison to previously used constructs (old linker, SPVAT; new linker, DGSPVAT). The DG-linker variant performed identically in β3 integrin spreading assays (Pinon et al., 2014), but showed slightly better clustering behavior in response to co-transfected kindlin-1 constructs (data not shown). A non-tagged mouse αv-integrin construct was amplified by PCR from a mouse placenta cDNA and cloned into pcDNA3 using the following primers (forward, 5′-ATTATGGATCCACCATGGCTGCTCCCGGGCG-CCTGCT-3′; reverse: 5′-ATATTAGGGCCCTCAGGTTTCAGAGTTCC-TT-3′) as described previously (Wiedle et al., 1999).

Transfections

Adherent (B16F1, COS7) or non-adherent cells (talin knockout), were transfected in 6-well culture dishes with the JET PEi transfection reagent (Polyplus-transfection) according to the manufacturer's protocol. For multiple transfections, different vector DNAs were mixed at equimolar concentrations. For adherent cells, the transfection mixture was removed and replaced with fresh medium after 6 h. For talin-knockout cells, the transfection mixture was left on the cells.

Integrin clustering analysis

After 6 h in transfection mixture, melanoma B16F1 cells were detached using trypsin-EDTA and plated on ethanol-sterilized glass-bottom dishes in FCS-containing culture medium. After 48 h on the FCS-coated glass surface, cells were either fixed directly, or after 20 min exposure to 0.5 mM Mn^{2+} in DMEM containing FCS, with 4% PFA (paraformaldehyde in PBS) for 10 min. Cells were subsequently immerged in PBS for total internal fluorescence microscopy. Integrin clustering analysis was then performed from TIRF images according to methods reported by Saltel et al. (2009). In brief, after background removal, an arbitrary threshold that allowed clustered and membrane-inserted integrins to be distinguished was used to quantify the area exhibiting integrin clusters relative to the total cell surface.

Integrin activation assay

48 h after transfection, mouse melanoma B16F1 cells were detached using non-enzymatic cell-dissociation solution (SIGMA C5788), and talin-knockout cells were collected using trypsin-EDTA, as described above, in culture medium. Cells were then washed twice in PBS containing 0.5 mg/ml BSA and split into two equal populations. Antibody staining or soluble-ligand incubation was performed on ice in PBS containing 0.5 mg/ml BSA. For one cell population, the total amount of cell-surface integrin was revealed by staining with either a hamster anti-β1-integrin antibody (clone HM β1-1; 550530, Pharmingen, BD) or hamster anti-β3-integrin antibody (anti-mouse CD61, clone 2C9.G2; 553344, Pharmingen, BD). The other cell population was stained with a conformation-specific rat monoclonal antibody (rat anti-mouse CD29, clone 9EG7, 553715, Pharmingen, BD) to detect the extended form of the β1 integrin (Lenter et al., 1993), or incubated with an RGD-containing fusion protein of the snake venom disintegrin (kistrin) and the first Ig domain of CD31 (SKI-7), followed by incubation with a rat anti-CD31 monoclonal antibody (GC51) as described previously (Saltel et al., 2009). Subsequent detection of the conformation-specific antibody or the bound β3 integrin ligand SKI-7–GC51 complex were achieved using PE-labeled affinity-purified anti-hamster antibody (127-115-160; Jackson ImmunoResearch Europe), or F(ab′)$_2$ fragments of goat anti-rat antibodies, respectively and analyzed in an Accuri flow cytometer. Integrin activation was determined by the ratio of the signal between the activation-specific and total integrin-binding antibodies as described in Saltel et al. (2009).

Cell-derived matrix

To prepare cell-derived matrix in ethanol-sterilized glass-bottom dishes, the dishes were coated for 60 min at 37°C with 0.2% gelatin in PBS then washed three times in PBS. The gelatin coating was fixed for 30 min in 1% glutaraldehyde, washed in PBS and blocked with 1 M glycine in PBS for 20 min, both at room temperature. After washing in PBS and equilibration in DMEM containing 10% FCS for 30 min at 37°C, 3T3 cells were plated at 50,000 cells/cm^2 and incubated until they reached confluency (typically, 1 day). The medium – DMEM containing 10% FCS, antibiotics and ascorbic acid at 50 µg/ml – was then changed daily. After 7 days of culture, the wells were washed with PBS and incubated in extraction buffer at 37°C (20 mM NH_4OH containing 0.5% Triton X-100 in PBS) for periods of 2 min. DNA of lysed cells was removed by DNAseI (Amersham, 10 U/ml final) treatment in PBS containing 0.5 mM Mg^{2+} and 1 mM Ca^{2+} at 37°C

for 30 min. After gentle washing with PBS containing 0.5 mM Mg^{2+} and 1 mM Ca^{2+}, the cell-derived matrix was blocked in DMEM containing 10% FCS for 30 min at 37°C, prior to seeding with talin-knockout cells transfected with GFP–talin constructs. After incubation for 6 h, invaded and spread cells were fixed in 4% PFA in PBS for 10 min and subsequently imaged in PBS by confocal or epifluorescence microscopy.

Cysteine crosslinking

COS7 cells were transfected in a 6-well plate using JetPEi reagent (1.5 µl; Polyplus-transfection) containing 0.3 µg of mouse αv integrin expression vector, 0.3 µg of mRFP–kindlin-1 vector, 0.3 µg of wild-type or cysteine-mutated β3–GFP integrin constructs (all in pcDNA3) and 0.3 µg of wild-type or cysteine-mutated CFP–talin head constructs, as described above. After 1 d, the culture medium was supplemented with 20 µg/ml 2-bromopalmitate for an additional 17 h, in order to prevent palmitoylation of juxtamembrane cysteine residues. Prior to cell extraction, cells were oxidized for 10 min at 4°C in 400 µl of DMEM medium containing 200 µM $CuSO_4$, 100 µM phenanthroline and 0.02% saponin. Cells were lysed after gentle removal of the oxidation solution in 300 µl of Tris-buffered saline containing 2% Triton X-100, 0.1% NP40, 5 mM N-ethylmaleimide, 1 mM PMSF and protease inhibitors at 1 µg/ml (chymotrypsin, leupeptine, aprotinin and pepstatin; Sigma) for 10 min at 4°C. 40 µl of the lysate was subsequently run on an SDS–PAGE gel (6%) under non-reducing conditions, then transferred to nitrocellulose and revealed using a mouse monoclonal anti-GFP antibody (clone B34, MMS-118R, LOT/147936001; Covance, Berkeley, CA) according to standard protocols. Analysis of the cysteine-crosslinked samples by 2D-SDS–PAGE (non-reduced/reduced) was performed as follows. The sample to be analysed in 2D was run alongside a pre-stained molecular weight marker on a 6% SDS–PAGE gel under non-reducing conditions. The sample band and part of the marker were then cut from the gel and placed on top of the stacking gel of a 10% SDS–PAGE gel. The gel slice was then overlaid with 1× sample buffer containing reducing agents. SDS–PAGE was stopped for 10 min once the front had just passed the gel slice, in order to reduce the included samples, and subsequently resolved. Transfer to nitrocellulose and anti-GFP detection was then performed as described above.

Small-angle X-ray scattering

Small angle X-ray scattering (SAXS) data for talins t1–405, t1–405(del30) and t1–405(del37/GAG) were collected at the P12 beamline at the PETRA III storage ring (EMBL Hamburg/DESY, Hamburg) (Blanchet et al., 2015). Analysis was performed on the monomeric fraction of the sample, as separated by in-line size exclusion chromatography. 100 µl of talin head in a concentration of 4.8–7.6 mg/ml in 50 mM sodium phosphate (pH 7.2) containing 150 mM NaCl was injected onto a Superdex 200 10/300 GL column with a flow rate of 0.25 ml/min. From the column, the sample flowed through the right-angle light-scattering detector at 26°C and through the SAXS sample cell at 10°C. SAXS data were collected on a Pilatus 2 M detector at a 3-m distance from the sample cell, at a wavelength of 1.24 Å, covering the momentum transfer range of $0.025<s<4.8$ Å^{-1}. Data were collected at 1-s intervals with an exposure time of 995 ms. The details of the experiment and data analyses are described in Table S5. The SAXS data has been deposited in the Small Angle Scattering Biological Data Bank and can be accessed at https://www.sasbdb.org/project/796/.

Statistics

Statistical analyses were carried out in GraphPad Prism 5.02 for Windows (GraphPad Software, La Jolla, CA). All clustering data were analyzed using one-way analysis of variance (ANOVA) and a Tukey's multiple comparison test for differences between the groups. The cell spreading data in Fig. 6B were analyzed using a two-tailed, unpaired *t*-test.

Acknowledgements

Ritva Romppanen, Ulla Kiiskinen, Niklas Kähkönen, Tatiana Fomekong and Monica Julio-Barreto are acknowledged for excellent technical help, and Michael Bachmann for help in figure preparations. Hongquan Zhang and Staffan Strömblad (Karolinska Institutet, Sweden) kindly provided the kindlin-1 construct. CSC – IT Center for Science Ltd. is acknowledged for computational resources, and Biocenter Finland is acknowledged for infrastructure support.

Competing interests

The authors declare no competing or financial interests.

Author contributions

Conceptualization: S.K., J.J., M.V., V.P.H., B.W.-H.; Methodology: S.K., L.A., P.Z., M.-C.J., M.v.E., A.T., M.L., X.L., A.O., J.J., J.A.E.M., M.V., I.V., T.R., D.S., J.W., V.P.H., B.W.-H.; Software: A.O., T.R., D.S.; Validation: S.K., A.T., D.S., J.W., V.P.H., B.W.-H; Formal analysis: S.K., M.-C.J., M.v.E., A.T., R.R., A.O., T.R., J.W., V.P.H.; Investigation: M.B., R.H.C., S.K., L.A., P.Z., M.-C.J., M.v.E., A.T., M.L., X.L., R.R., A.O., J.J., J.A.E.M., T.R., V.P.H., B.W.-H.; Resources: J.J., I.V., D.S., J.W., V.P.H., B.W.-H.; Data curation: S.K., L.A., P.Z., M.-C.J., M.v.E., A.T., X.L., R.R., M.V., T.R., V.P.H., B.W.-H.; Writing - original draft: S.K., V.P.H., B.W.-H.; Writing - review & editing: S.K., L.A., P.Z., M.v.E., A.T., X.L., R.R., A.O., J.J., J.A.E.M., M.V., I.V., T.R., J.W., V.P.H., B.W.-H.; Visualization: S.K., P.Z., J.J., T.R., B.W.-H.; Supervision: R.H.C., J.J., M.V., I.V., T.R., D.S., J.W., V.P.H., B.W.-H.; Project administration: J.W., V.P.H., B.W.-H.; Funding acquisition: V.P.H., B.W.-H.

Funding

We acknowledge Academy of Finland (grant number 290506) for research funding. This work was granted access to the HPC resources of EPCC made available within the Distributed European Computing Initiative by the PRACE-2IP, receiving funding from the European Community's Seventh Framework Programme (FP7/2007–2013) under grant agreement number RI-283493. S.K. was supported by the Tampere Graduate Program in Biomedicine and Biotechnology. B.W.-H. and M.-C.J. were supported by a grant from the Schweizerischer Nationalfonds zur Förderung der Wissenschaftlichen Forschung (31003A_166384).

Data availability

Molecular dynamics data have been deposited into IDA research data storage and can be accessed via https://etsin.fairdata.fi/dataset/4bf3cf43-49f4-4898-bf38-0381552c3fd2. Small-angle x-ray scattering data have been deposited in the Small Angle Scattering Biological Data Bank, and can be accessed via https://www.sasbdb.org/project/796/.

Supplementary information

Supplementary information available online at
https://jcs.biologists.org/lookup/doi/10.1242/jcs.239202.supplemental

References

Anthis, N. J. and Campbell, I. D. (2011). The tail of integrin activation. *Trends Biochem. Sci.* **36**, 191-198. doi:10.1016/j.tibs.2010.11.002

Anthis, N. J., Wegener, K. L., Ye, F., Kim, C., Goult, B. T., Lowe, E. D., Vakonakis, I., Bate, N., Critchley, D. R., Ginsberg, M. H. et al. (2009). The structure of an integrin/talin complex reveals the basis of inside–out signal transduction. *EMBO J.* **28**, 3623-3632. doi:10.1038/emboj.2009.287

Anthis, N. J., Wegener, K. L., Critchley, D. R. and Campbell, I. D. (2010). Structural diversity in integrin/talin interactions. *Structure* **18**, 1654-1666. doi:10.1016/j.str.2010.09.018

Bachmann, M., Kukkurainen, S., Hytönen, V. P. and Wehrle-Haller, B. (2019). Cell Adhesion by Integrins. *Physiol. Rev.* **99**, 1655-1699. doi:10.1152/physrev.00036.2018

Ballestrem, C., Wehrle-Haller, B. and Imhof, B. A. (1996). Actin dynamics in living mammalian cells. *J. Cell Sci.* **111**, 1649-1658.

Ballestrem, C., Hinz, B., Imhof, B. A. and Wehrle-Haller, B. (2001). Marching at the front and dragging behind. *J. Cell Biol.* **155**, 1319-1332. doi:10.1083/jcb.200107107

Blanchet, C. E., Spilotros, A., Schwemmer, F., Graewert, M. A., Kikhney, A., Jeffries, C. M., Franke, D., Mark, D., Zengerle, R., Cipriani, F. et al. (2015). Versatile sample environments and automation for biological solution X-ray scattering experiments at the P12 beamline (PETRA III, DESY). *J. Appl. Crystallogr.* **48**, 431-443. doi:10.1107/S160057671500254X

Bouaouina, M., Lad, Y. and Calderwood, D. A. (2008). The N-terminal domains of talin cooperate with the phosphotyrosine binding-like domain to activate β1 and β3 integrins. *J. Biol. Chem.* **283**, 6118-6125. doi:10.1074/jbc.M709527200

Bouaouina, M., Goult, B. T., Huet-Calderwood, C., Bate, N., Brahme, N. N., Barsukov, I. L., Critchley, D. R. and Calderwood, D. A. (2012). A conserved lipid-binding loop in the kindlin FERM F1 domain is required for kindlin-mediated αIIbβ3 integrin coactivation. *J. Biol. Chem.* **287**, 6979-6990. doi:10.1074/jbc.M111.330845

Bromberger, T., Klapproth, S., Rohwedder, I., Zhu, L., Mittmann, L., Reichel, C. A., Sperandio, M., Qin, J. and Moser, M. (2018). Direct Rap1/Talin1 interaction regulates platelet and neutrophil integrin activity in mice. *Blood.* **132**, 2754-2762. doi:10.1182/blood-2018-04-846766

Bullock, J. M. A., Schwab, J., Thalassinos, K. and Topf, M. (2016). The importance of non-accessible crosslinks and solvent accessible surface distance in modeling proteins with restraints from crosslinking mass spectrometry. *Mol. Cell. Proteomics* **15**, 2491-2500. doi:10.1074/mcp.M116.058560

Bunch, T. A. (2009). Integrin αIIbβ3 activation in chinese hamster ovary cells and platelets increases clustering rather than affinity. *J. Biol. Chem.* **285**, 1841-1849. doi:10.1074/jbc.M109.057349

Calderwood, D. A., Yan, B., de Pereda, J. M., Alvarez, B. G., Fujioka, Y., Liddington, R. C. and Ginsberg, M. H. (2002). The phosphotyrosine binding-like domain of talin activates integrins. *J. Biol. Chem.* **277**, 21749-21758. doi:10.1074/jbc.M111996200

Calderwood, D. A., Campbell, I. D. and Critchley, D. R. (2013). Talins and kindlins: partners in integrin-mediated adhesion. *Nat. Rev. Mol. Cell Biol.* **14**, 503-517. doi:10.1038/nrm3624

Camp, D., Haage, A., Solianova, V., Castle, W. M., Xu, Q. A., Lostchuck, E., Goult, B. T. and Tanentzapf, G. (2018). Direct binding of Talin to Rap1 is required for cell-ECM adhesion in Drosophila. *J. Cell Sci.* **131**, jcs225144. doi:10.1242/jcs.225144

Changede, R., Xu, X., Margadant, F. and Sheetz, M. P. (2015). Nascent integrin adhesions form on all matrix rigidities after integrin activation. *Dev. Cell.* **35**, 614-621. doi:10.1016/j.devcel.2015.11.001

Chen, V. B., Arendall, W. B., III, Headd, J. J., Keedy, D. A., Immormino, R. M., Kapral, G. J., Murray, L. W., Richardson, J. S. and Richardson, D. C. (2010). *MolProbity* : all-atom structure validation for macromolecular crystallography. *Acta Crystallogr. Sect. D Biol. Crystallogr.* **66**, 12-21. doi:10.1107/S0907444909042073

Chinthalapudi, K., Rangarajan, E. S. and Izard, T. (2018). The interaction of talin with the cell membrane is essential for integrin activation and focal adhesion formation. *Proc. Natl. Acad. Sci. USA* **115**, 10339-10344. doi:10.1073/pnas.1806275115

Cluzel, C., Saltel, F., Lussi, J., Paulhe, F., Imhof, B. A. and Wehrle-Haller, B. (2005). The mechanisms and dynamics of αvβ3 integrin clustering in living cells. *J. Cell Biol.* **171**, 383-392. doi:10.1083/jcb.200503017

Debrand, E., Conti, F. J., Bate, N., Spence, L., Mazzeo, D., Pritchard, C. A., Monkley, S. J. and Critchley, D. R. (2012). Mice carrying a complete deletion of the talin2 coding sequence are viable and fertile. *Biochem. Biophys. Res. Commun.* **426**, 190-195. doi:10.1016/j.bbrc.2012.08.061

Do, C. B., Mahabhashyam, M. S. P., Brudno, M. and Batzoglou, S. (2005). ProbCons: Probabilistic consistency-based multiple sequence alignment. *Genome Res.* **15**, 330-340. doi:10.1101/gr.2821705

Elliott, P. R., Goult, B. T., Kopp, P. M., Bate, N., Grossmann, J. G., Roberts, G. C. K., Critchley, D. R. and Barsukov, I. L. (2010). The structure of the talin head reveals a novel extended conformation of the FERM domain. *Structure* **18**, 1289-1299. doi:10.1016/j.str.2010.07.011

Ellis, S. J., Goult, B. T., Fairchild, M. J., Harris, N. J., Long, J., Lobo, P., Czerniecki, S., Van Petegem, F., Schöck, F., Peifer, M. et al. (2013). Talin autoinhibition is required for morphogenesis. *Curr. Biol.* **23**, 1825-1833. doi:10.1016/j.cub.2013.07.054

Eng, E. T., Smagghe, B. J., Walz, T. and Springer, T. A. (2011). Intact α_{IIb} β_3 integrin is extended after activation as measured by solution X-ray scattering and electron microscopy. *J. Biol. Chem.* **286**, 35218-35226. doi:10.1074/jbc.M111.275107

Feigelson, S. W., Grabovsky, V., Manevich-Mendelson, E., Pasvolsky, R., Shulman, Z., Shinder, V., Klein, E., Etzioni, A., Aker, M. and Alon, R. (2011). Kindlin-3 is required for the stabilization of TCR-stimulated LFA-1:ICAM-1 bonds critical for lymphocyte arrest and spreading on dendritic cells. *Blood* **117**, 7042-7052. doi:10.1182/blood-2010-12-322859

Feng, C., Li, Y.-F., Yau, Y.-H., Lee, H.-S., Tang, X.-Y., Xue, Z.-H., Zhou, Y.-C., Lim, W.-M., Cornvik, T. C., Ruedl, C. et al. (2012). Kindlin-3 mediates integrin αLβ2 outside-in signaling, and it interacts with scaffold protein receptor for activated-C kinase 1 (RACK1). *J. Biol. Chem.* **287**, 10714-10726. doi:10.1074/jbc.M111.299594

García-Alvarez, B., de Pereda, J. M., Calderwood, D. A., Ulmer, T. S., Critchley, D. R., Campbell, I. D., Ginsberg, M. H. and Liddington, R. C. (2003). Structural determinants of integrin recognition by talin. *Mol. Cell* **11**, 49-58. doi:10.1016/S1097-2765(02)00823-7

Gingras, A. R., Bate, N., Goult, B. T., Hazelwood, L., Canestrelli, I., Grossmann, J. G., Liu, H. J., Putz, N. S. M., Roberts, G. C. K., Volkmann, N. et al. (2008). The structure of the C-terminal actin-binding domain of talin. *EMBO J.* **27**, 458-469. doi:10.1038/sj.emboj.7601965

Gingras, A. R., Lagarrigue, F., Cuevas, M. N., Valadez, A. J., Zorovich, M., McLaughlin, W., Lopez-Ramirez, M. A., Seban, N., Ley, K., Kiosses, W. B. et al. (2019). Rap1 binding and a lipid-dependent helix in talin F1 domain promote integrin activation in tandem. *J. Cell Biol.* **218**, 1799-1809. doi:10.1083/jcb.201810061

Goksoy, E., Ma, Y.-Q., Wang, X., Kong, X., Perera, D., Plow, E. F. and Qin, J. (2008). Structural basis for the autoinhibition of talin in regulating integrin activation. *Mol. Cell* **31**, 124-133. doi:10.1016/j.molcel.2008.06.011

Goult, B. T., Bouaouina, M., Elliott, P. R., Bate, N., Patel, B., Gingras, A. R., Grossmann, J. G., Roberts, G. C. K., Calderwood, D. A., Critchley, D. R. et al. (2010). Structure of a double ubiquitin-like domain in the talin head: a role in integrin activation. *EMBO J.* **29**, 1069-1080. doi:10.1038/emboj.2010.4

Goult, B. T., Xu, X.-P., Gingras, A. R., Swift, M., Patel, B., Bate, N., Kopp, P. M., Barsukov, I. L., Critchley, D. R., Volkmann, N. et al. (2013). Structural studies on full-length talin1 reveal a compact auto-inhibited dimer: implications for talin activation. *Hybrid Methods Macromol. Struct.* **184**, 21-32. doi:10.1016/j.jsb.2013.05.014

Haining, A. W. M., Lieberthal, T. J. and del Río Hernández, A. (2016). Talin: a mechanosensitive molecule in health and disease. *FASEB J.* **30**, 2073-2085. doi:10.1096/fj.201500080R

Harburger, D. S., Bouaouina, M. and Calderwood, D. A. (2009). Kindlin-1 and –2 directly bind the C-terminal region of β integrin cytoplasmic tails and exert integrin-specific activation effects. *J. Biol. Chem.* **284**, 11485-11497. doi:10.1074/jbc.M809233200

Hemmings, L., Rees, D. J. G., Ohanian, V., Bolton, S. J., Gilmore, A. P., Patel, B., Priddle, H., Trevithick, J. E., Hynes, R. O. and Critchley, D. R. (1996). Talin contains three actin-binding sites each of which is adjacent to a vinculin-binding site. *J. Cell Sci.* **109**, 2715-2726.

Hughes, P. E., Diaz-Gonzalez, F., Leong, L., Wu, C., McDonald, J. A., Shattil, S. J. and Ginsberg, M. H. (1996). Breaking the Integrin Hinge: A defined structural constraint regulates integrin signaling. *J. Biol. Chem.* **271**, 6571-6574. doi:10.1074/jbc.271.12.6571

Hynes, R. O. (2002). Integrins: bidirectional, allosteric signaling machines. *Cell* **110**, 673-687. doi:10.1016/S0092-8674(02)00971-6

Jorgensen, W. L., Maxwell, D. S. and Tirado-Rives, J. (1996). Development and testing of the OPLS all-atom force field on conformational energetics and properties of organic liquids. *J. Am. Chem. Soc.* **118**, 11225-11236. doi:10.1021/ja9621760

Kalli, A. C., Campbell, I. D. and Sansom, M. S. P. (2013). Conformational changes in talin on binding to anionic phospholipid membranes facilitate signaling by integrin transmembrane helices. *PLoS Comput. Biol.* **9**, e1003316. doi:10.1371/journal.pcbi.1003316

Kang, B. S., Cooper, D. R., Devedjiev, Y., Derewenda, U. and Derewenda, Z. S. (2002). The structure of the FERM domain of merlin, the neurofibromatosis type 2 gene product. *Acta Crystallogr. Sect. D.* **58**, 381-391. doi:10.1107/S0907444901021175

Katzemich, A., Long, J. Y., Panneton, V., Fisher, L. A. B., Hipfner, D. and Schöck, F. (2019). Slik phosphorylation of Talin T152 is crucial for proper Talin recruitment and maintenance of muscle attachment in Drosophila. *Development* **146**, dev176339. doi:10.1242/dev.176339

Kumar, S., Stecher, G. and Tamura, K. (2016). MEGA7: molecular evolutionary genetics analysis version 7.0 for bigger datasets. *Mol. Biol. Evol.* **33**, 1870-1874. doi:10.1093/molbev/msw054

Lagarrigue, F., Gingras, A. R., Paul, D. S., Valadez, A. J., Cuevas, M. N., Sun, H., Lopez-Ramirez, M. A., Goult, B. T., Shattil, S. J., Bergmeier, W. et al. (2018). Rap1 binding to the talin 1 F0 domain makes a minimal contribution to murine platelet GPIIb-IIIa activation. *Blood Adv.* **2**, 2358-2368. doi:10.1182/bloodadvances.2018020487

Lenter, M., Uhlig, H., Hamann, A., Jenö, P., Imhof, B. and Vestweber, D. (1993). A monoclonal antibody against an activation epitope on mouse integrin chain beta 1 blocks adhesion of lymphocytes to the endothelial integrin alpha 6 beta 1. *Proc. Natl. Acad. Sci. USA* **90**, 9051-9055. doi:10.1073/pnas.90.19.9051

Li, H., Deng, Y., Sun, K., Yang, H., Liu, J., Wang, M., Zhang, Z., Lin, J., Wu, C., Wei, Z. et al. (2017). Structural basis of kindlin-mediated integrin recognition and activation. *Proc. Natl. Acad. Sci. USA* **114**, 9349-9354. doi:10.1073/pnas.1703064114

Lu, S., Fan, S.-B., Yang, B., Li, Y.-X., Meng, J.-M., Wu, L., Li, P., Zhang, K., Zhang, M.-J., Fu, Y. et al. (2015). Mapping native disulfide bonds at a proteome scale. *Nat. Methods.* **12**, 329-331. doi:10.1038/nmeth.3283

Ma, Y.-Q., Qin, J., Wu, C. and Plow, E. F. (2008). Kindlin-2 (Mig-2): a co-activator of β3 integrins. *J. Cell Biol.* **181**, 439-446. doi:10.1083/jcb.200710196

Monkley, S. J., Zhou, X.-H., Kinston, S. J., Giblett, S. M., Hemmings, L., Priddle, H., Brown, J. E., Pritchard, C. A., Critchley, D. R. and Fässler, R. (2000). Disruption of the talin gene arrests mouse development at the gastrulation stage. *Dev. Dyn.* **219**, 560-574. doi:10.1002/1097-0177(2000)9999:9999<::AID-DVDY1079>3.0.CO;2-Y

Monkley, S. J., Kostourou, V., Spence, L., Petrich, B., Coleman, S., Ginsberg, M. H., Pritchard, C. A. and Critchley, D. R. (2011). Endothelial cell talin1 is essential for embryonic angiogenesis. *Dev. Biol.* **349**, 494-502. doi:10.1016/j.ydbio.2010.11.010

Montanez, E., Ussar, S., Schifferer, M., Bösl, M., Zent, R., Moser, M. and Fässler, R. (2008). Kindlin-2 controls bidirectional signaling of integrins. *Genes Dev.*. **22**, 1325-1330. doi:10.1101/gad.469408

Moore, D. T., Nygren, P., Jo, H., Boesze-Battaglia, K., Bennett, J. S. and DeGrado, W. F. (2012). Affinity of talin-1 for the β3-integrin cytosolic domain is modulated by its phospholipid bilayer environment. *Proc. Natl. Acad. Sci. USA* **109**, 793-798. doi:10.1073/pnas.1117220108

Moser, M., Nieswandt, B., Ussar, S., Pozgajova, M. and Fässler, R. (2008). Kindlin-3 is essential for integrin activation and platelet aggregation. *Nat. Med.* **14**, 325-330. doi:10.1038/nm1722

Moser, M., Bauer, M., Schmid, S., Ruppert, R., Schmidt, S., Sixt, M., Wang, H.-V., Sperandio, M. and Fässler, R. (2009). Kindlin-3 is required for β2 integrin-mediated leukocyte adhesion to endothelial cells. *Nat. Med.* **15**, 300-305. doi:10.1038/nm.1921

Mould, A. P., Akiyama, S. K. and Humphries, M. J. (1995). Regulation of integrin α5β1-fibronectin interactions by divalent cations: evidence for distinct classes of binding sites Mn2+, Mg2+, and Ca2+. *J. Biol. Chem.* **270**, 26270-26277. doi:10.1074/jbc.270.44.26270

O'Connell, K. L. and Stults, J. T. (1997). Identification of mouse liver proteins on two-dimensional electrophoresis gels by matrix-assisted laser desorption/ionization mass spectrometry of in situ enzymatic digests. *Electrophoresis.* **18**, 349-359. doi:10.1002/elps.1150180309

Orłowski, A., Kukkurainen, S., Pöyry, A., Rissanen, S., Vattulainen, I., Hytönen, V. P. and Róg, T. (2015). PIP2 and Talin Join Forces to Activate Integrin. *J. Phys. Chem. B.* **119**, 12381-12389. doi:10.1021/acs.jpcb.5b06457

Pinon, P., Pärssinen, J., Vazquez, P., Bachmann, M., Rahikainen, R., Jacquier, M.-C., Azizi, L., Määttä, J. A., Bastmeyer, M., Hytönen, V. P. et al. (2014). Talin-bound NPLY motif recruits integrin-signaling adapters to regulate cell spreading and mechanosensing. *J. Cell Biol.* **205**, 265-281. doi:10.1083/jcb.201308136

Qu, H., Tu, Y., Shi, X., Larjava, H., Saleem, M. A., Shattil, S. J., Fukuda, K., Qin, J., Kretzler, M. and Wu, C. (2011). Kindlin-2 regulates podocyte adhesion and fibronectin matrix deposition through interactions with phosphoinositides and integrins. *J. Cell Sci.* **124**, 879-891. doi:10.1242/jcs.076976

Rangarajan, E. S., Primi M. C., Colgan, L. A., Chinthalapudi, K., Yasuda, R. and Izard, T. (2020). A distinct talin2 structure directs isoform specificity in cell adhesion. *J. Biol. Chem.* **295**, 12885-12899. doi:10.1074/jbc.RA119.010789

Rees, D. J. G., Ades, S. E., Singer, S. J. and Hynes, R. O. (1990). Sequence and domain structure of talin. *Nature* **347**, 685-689. doi:10.1038/347685a0

Roberts, G. C. K. and Critchley, D. R. (2009). Structural and biophysical properties of the integrin-associated cytoskeletal protein talin. *Biophys. Rev.* **1**, 61-69. doi:10.1007/s12551-009-0009-4

Rognoni, E., Ruppert, R. and Fässler, R. (2016). The kindlin family: functions, signaling properties and implications for human disease. *J. Cell Sci.* **129**, 17-27. doi:10.1242/jcs.161190

Šali, A. and Blundell, T. L. (1993). Comparative protein modelling by satisfaction of spatial restraints. *J. Mol. Biol.* **234**, 779-815. doi:10.1006/jmbi.1993.1626

Saltel, F., Mortier, E., Hytönen, V. P., Jacquier, M.-C., Zimmermann, P., Vogel, V., Liu, W. and Wehrle-Haller, B. (2009). New PI(4,5)P2- and membrane proximal integrin–binding motifs in the talin head control β3-integrin clustering. *J. Cell Biol.* **187**, 715-731. doi:10.1083/jcb.200908134

Schmidt, S., Nakchbandi, I., Ruppert, R., Kawelke, N., Hess, M. W., Pfaller, K., Jurdic, P., Fässler, R. and Moser, M. (2011). Kindlin-3-mediated signaling from multiple integrin classes is required for osteoclast-mediated bone resorption. *J. Cell Biol.* **192**, 883-897. doi:10.1083/jcb.201007141

Senetar, M. A. and McCann, R. O. (2005). Gene duplication and functional divergence during evolution of the cytoskeletal linker protein talin. *Gene.* **362**, 141-152. doi:10.1016/j.gene.2005.08.012

Senetar, M. A., Moncman, C. L. and McCann, R. O. (2007). Talin2 is induced during striated muscle differentiation and is targeted to stable adhesion complexes in mature muscle. *Cell Motil. Cytoskelet.* **64**, 157-173. doi:10.1002/cm.20173

Song, X., Yang, J., Hirbawi, J., Ye, S., Perera, H. D., Goksoy, E., Dwivedi, P., Plow, E. F., Zhang, R. and Qin, J. (2012). A novel membrane-dependent on/off switch mechanism of talin FERM domain at sites of cell adhesion. *Cell Res.* **22**, 1533-1545. doi:10.1038/cr.2012.97

Soto-Ribeiro, M., Kastberger, B., Bachmann, M., Azizi, L., Fouad, K., Jacquier, M.-C., Boettiger, D., Bouvard, D., Bastmeyer, M., Hytönen, V. P. et al. (2019). β1D integrin splice variant stabilizes integrin dynamics and reduces integrin signaling by limiting paxillin recruitment. *J. Cell Sci.* **132**, jcs224493. doi:10.1242/jcs.224493

Sun, Z., Guo, S. S. and Fässler, R. (2016). Integrin-mediated mechanotransduction. *J. Cell Biol.* **215**, 445-456. doi:10.1083/jcb.201609037

Tadokoro, S., Shattil, S. J., Eto, K., Tai, V., Liddington, R. C., de Pereda, J. M., Ginsberg, M. H. and Calderwood, D. A. (2003). Talin binding to integrin beta tails: a final common step in integrin activation. *Science* **302**, 103-106. doi:10.1126/science.1086652

Theodosiou, M., Widmaier, M., Böttcher, R. T., Rognoni, E., Veelders, M., Bharadwaj, M., Lambacher, A., Austen, K., Müller, D. J., Zent, R. et al. (2016). Kindlin-2 cooperates with talin to activate integrins and induces cell spreading by directly binding paxillin. *eLife* **5**, e10130. doi:10.7554/eLife.10130

Tria, G., Mertens, H. D. T., Kachala, M. and Svergun, D. I. (2015). Advanced ensemble modelling of flexible macromolecules using X-ray solution scattering. *IUCrJ* **2**, 207-217. doi:10.1107/S205225251500202X

Van Der Spoel, D., Lindahl, E., Hess, B., Groenhof, G., Mark, A. E. and Berendsen, H. J. C. (2005). GROMACS: Fast, flexible, and free. *J. Comput. Chem.* **26**, 1701-1718. doi:10.1002/jcc.20291

Waterhouse, A. M., Procter, J. B., Martin, D. M. A., Clamp, M. and Barton, G. J. (2009). Jalview Version 2–a multiple sequence alignment editor and analysis workbench. *Bioinformatics* **25**, 1189-1191. doi:10.1093/bioinformatics/btp033

Wegener, K. L., Partridge, A. W., Han, J., Pickford, A. R., Liddington, R. C., Ginsberg, M. H. and Campbell, I. D. (2007). Structural basis of integrin activation by Talin. *Cell.* **128**, 171-182. doi:10.1016/j.cell.2006.10.048

Wiedle, G., Johnson-Léger, C. and Imhof, B. A. (1999). A chimeric cell adhesion molecule mediates homing of lymphocytes to vascularized tumors. *Cancer Res.* **59**, 5255-5263.

Xing, B., Thuppal, S., Jedsadayanmata, A., Du, X. and Lam, S. C.-T. (2006). TA205, an anti-talin monoclonal antibody, inhibits integrin–talin interaction. *FEBS Lett.* **580**, 2027-2032. doi:10.1016/j.febslet.2006.02.077

Ye, F., Petrich, B. G., Anekal, P., Lefort, C. T., Kasirer-Friede, A., Shattil, S. J., Ruppert, R., Moser, M., Fässler, R. and Ginsberg, M. H. (2013). The mechanism of kindlin-mediated activation of integrin αIIbβ3. *Curr. Biol.* **23**, 2288-2295. doi:10.1016/j.cub.2013.09.050

Ye, X., McLean, M. A. and Sligar, S. G. (2016). Phosphatidylinositol 4,5-bisphosphate modulates the affinity of talin-1 for phospholipid bilayers and activates its autoinhibited form. *Biochemistry* **55**, 5038-5048. doi:10.1021/acs.biochem.6b00497

Zhang, H., Chang, Y.-C., Huang, Q., Brennan, M. L. and Wu, J. (2016). Structural and functional analysis of a talin triple-domain module suggests an alternative talin autoinhibitory configuration. *Structure* **24**, 721-729. doi:10.1016/j.str.2016.02.020

Zhu, L., Yang, J., Bromberger, T., Holly, A., Lu, F., Liu, H., Sun, K., Klapproth, S., Hirbawi, J., Byzova, T. V. et al. (2017). Structure of Rap1b bound to talin reveals a pathway for triggering integrin activation. *Nat. Commun.* **8**, 1744. doi:10.1038/s41467-017-01822-8